



*Citation for published version:*

Stringer, RM, Hillis, AJ & Zang, J 2016, 'Numerical investigation of laboratory tested cross-flow tidal turbines and Reynolds number scaling', *Renewable Energy*, vol. 85, pp. 1316-1327.  
<https://doi.org/10.1016/j.renene.2015.07.081>

*DOI:*

[10.1016/j.renene.2015.07.081](https://doi.org/10.1016/j.renene.2015.07.081)

*Publication date:*

2016

*Document Version*

Peer reviewed version

[Link to publication](#)

*Publisher Rights*

CC BY-NC-ND

## University of Bath

### General rights

Copyright and moral rights for the publications made accessible in the public portal are retained by the authors and/or other copyright owners and it is a condition of accessing publications that users recognise and abide by the legal requirements associated with these rights.

### Take down policy

If you believe that this document breaches copyright please contact us providing details, and we will remove access to the work immediately and investigate your claim.

1 **Numerical Investigation of Laboratory Tested Cross-Flow Tidal Turbines and Reynolds**  
2 **Number Scaling**

3

4 R. M. Stringer<sup>a</sup> (corresponding author), A. J. Hillis<sup>b</sup>, J. Zang<sup>a</sup>

5 <sup>a</sup> Department of Architecture and Civil Engineering, University of Bath, Bath, BA2 7AY, UK

6 <sup>b</sup> Department of Mechanical Engineering, University of Bath, Bath, BA2 7AY, UK

7 Contact: R. M. Stringer<sup>a</sup> Tel: +44 (0)1225 386621 Email: r.m.stringer@bath.ac.uk

8

9 **Abstract**

10 The cross-flow, or vertical axis tidal turbine, is a prominent configuration of marine  
11 renewable energy device aimed at converting tidal currents into electrical energy. This paper  
12 highlights the hydrodynamic limitations of laboratory testing such devices and uses numerical  
13 simulation to explore the effect of device scaling. Using a 2D Reynolds-Averaged Navier-  
14 Stokes (RANS) numerical approach, a single turbine blade is initially modelled and validated  
15 against published data. The resultant numerical model is then expanded to emulate an  
16 experimental cross-flow tidal turbine designed and tested by the University of Oxford. The  
17 simulated turbine achieves a close quantitative match for coefficients of power, torque and  
18 thrust, forming the basis of a study exploring the effects of Reynolds number scaling in three  
19 alternative operating conditions. It is discovered that the coefficient of power ( $C_p$ ) increases  
20 with  $\overline{Re}$  without a ubiquitous correlation until an  $\overline{Re}$  of  $\sim 350,000$ . Above this  $\overline{Re}$  the  $C_p$   
21 values for all three operation conditions become both proportional and predictable. The study  
22 represents a significant contribution to understanding the application of detailed numerical  
23 modelling techniques to cross-flow tidal turbines. The findings, with regard to scaling from  
24 laboratory data, could reduce uncertainty and development costs for new and existing devices.

25

26 **Keywords:** Cross-flow; Low Reynolds number; Numerical; RANS; Scaling; Tidal turbine

27

28

29 **1. Introduction**

30

31 The global requirement for clean, economically attractive energy has inspired many  
32 innovative tidal energy devices. One such variant, the cross-flow configuration, is explored in  
33 this study. This format of device has received growing interest from both academia and  
34 industry alike, with leading examples including the University of Oxford ‘THAWT’ device  
35 (now Kepler Energy) [1], and Italian developer Ponti di Archimede Internantional’s ‘Kobold’  
36 turbine [2]. Specifically, the device investigated here is a fixed pitch transverse turbine,  
37 designed and experimentally tested by the University of Oxford at laboratory scale. This type  
38 of experimental test is typical in the development of any tidal device in order to confirm  
39 theoretical and numerical predictions of its proposed hydrodynamic performance. However,  
40 downscaling is a complex issue, with reduced turbine performance a common issue due to a  
41 number of hydrodynamic effects.

42 It is well documented that lifting surface performance, namely its lift and drag  
43 characteristics, significantly declines at low blade chord Reynolds numbers ( $Re$ ). In addition,  
44 the flow behaviour around many standard foils below a Reynolds number of  $\sim 10^5$  becomes  
45 rapidly unstable due to a transitional boundary layer. These two factors contribute to the  
46 uncertainty of performance scaling particularly in the case of the cross-flow turbine where  
47 upstream and downstream blade performance is inherently coupled. Based on this premise,  
48 the research presented identifies and explores a number of hydrodynamic limitations of  
49 laboratory scale testing of cross-flow tidal turbines. A review of articles on the topic of low  
50  $Re$  conditions, both experimental and numerical, is presented and used to inform the  
51 numerical strategy of the research.

52 Using a defined numerical methodology, a mesh sensitivity study is completed for an  
53 isolated blade profile in order to assess and maximise the quantitative comparability at lab  
54 scale Reynolds numbers. The resulting numerical environment is modified to encompass a 2-  
55 dimensional version of the full experimental turbine which is tested at a number of tip speed  
56 ratios for validation against experimental data. Finally, the model is used to explore torque,

57 power and thrust outputs for the turbine at increasing diameters up to full scale. Results are  
 58 plotted against a mean Reynolds number, the intentionally isolated variable, to explore its  
 59 effects on performance.

60

### 61 **1.1 Turbine basics**

62

63 The concept of the cross-flow device originates from Darrieus' 1931 patent for a wind turbine  
 64 [3], the theory of which remains applicable to tidal turbines today. Fig. 1 depicts a cross-  
 65 section of a three bladed cross-flow turbine where the circular line is the blade's flight path  
 66 around rotational axis  $z$ . The direction of rotation is anti-clockwise at angular velocity  $\omega$ , at  
 67 radius  $r$ , the multiplication of which results in tangential velocity  $U_t$ . Components of the  
 68 oncoming free-stream velocity vector  $U_\infty$  and  $U_t$  are summed to give local velocity  $U$ , as  
 69 shown in (1), with the average value for one revolution  $\bar{U}$  given in (2). Assuming zero losses  
 70 at the downstream side of the turbine (omitting wake and induction factor losses),  $\alpha$  can be  
 71 calculated using (3), where  $\theta$  is the azimuth position of the blade as shown in Fig. 1. A key  
 72 relationship in turbine design, linking free-stream and rotation velocities, is the tip speed ratio  
 73 (TSR) or  $\lambda$ , as calculated by (4). This relationship is shown in Fig. 2, where  $\alpha$  is plotted with  
 74 increasing  $\theta$  for  $\lambda$  values of 2, 3 and 4. Operation of the turbine results from the vector sum of  
 75 the lift  $L$  and drag  $D$  supplying positive torque to the rotating system.

76

$$U = \sqrt{(U_\infty \sin \theta)^2 + (U_\infty \cos \theta + U_t)^2} = \frac{U_\infty \sin \theta}{\sin \alpha} \quad (1)$$

where  $U_\infty$  is a function of depth ( $h$ )

$$\bar{U} = \frac{1}{2\pi} \int_0^{2\pi} U d\theta \quad (2)$$

$$\alpha = \tan^{-1} \frac{U_\infty \sin \theta}{U_\infty \cos \theta + U_t} \equiv \tan^{-1} \frac{\sin \theta}{\cos \theta + \lambda} \quad (3)$$

$$TSR = \lambda = \frac{U_t}{U_\infty} \quad (4)$$

$$Re = \frac{\rho U c}{\mu} \quad (5)$$

$$\overline{Re} = \frac{\rho \overline{U} c}{\mu} \quad (6)$$

77

78 Evaluating Fig. 2, it is shown that as  $\lambda$  is increased, peak  $\alpha$  is decreased and vice versa. The  
 79 result is that a turbine blade experiences a fluctuating velocity  $U$  as a function of the boundary  
 80 condition  $U_\infty$ , operating condition  $\lambda$ , and instantaneous position  $\theta$ . Local velocity  $U$   
 81 determines the blade chord Reynolds number  $Re$ , as calculated by (5); where  $\rho$  is fluid  
 82 density,  $\mu$  is dynamic viscosity and  $c$  is blade chord length.  $Re$  is a non-dimensional value  
 83 representing the relative contributions of inertial and viscous forces acting on the blade, the  
 84 result of which determines its lift and drag curves, as discussed in section 2. With both  
 85 absolute and relative values of lift and drag being the primary factors in total turbine  
 86 performance, Reynolds number provides a suitable factor against which tidal turbines can be  
 87 characterised, with Froude number ( $Fr$ ) becoming increasingly important for high blockage,  
 88 near-surface or surface piecing devices [4]. With both Reynolds and Froude numbers being  
 89 impossible to satisfy simultaneously over large changes in scale [5], Reynolds number has  
 90 been chosen for investigation in the current study.

91 As  $Re$  is an instantaneous value, a mean value for one revolution of the turbine,  $\overline{Re}$ , is  
 92 used in this research as the independent variable against which turbine performance is  
 93 equated. The calculation of  $\overline{Re}$ , given in (6), is not corrected for streamwise induction losses  
 94 due to the uncertainty of its application for high level resolution models as used in this  
 95 research. For example, an induction factor loss applied uniformly across the rotor does not  
 96 account for varying performance of the blades throughout the upstream rotation and hence  
 97 would not result in reliable velocity corrections for the downstream positions. Additionally,  
 98 an attempt to establish a value for  $U_\infty$  for any given downstream location would require a  
 99 specified position upstream of the blade to be identified. With the flow velocity subject to

100 high gradients both spatially and temporally, selection of a position too close to the blade and  
101 the velocity may already be affected by its wake. Conversely, selection of a position too far  
102 from the blade and the velocity is likely to be unrepresentative of the actual flow the blade  
103 experiences. A robust approach for highly resolved numerical models is needed if a  
104 correction is to be of value, an issue which is currently the subject of ongoing research.

105

## 106 **1.2 Experiment Summary**

107

108 The benchmark for the numerical model is a laboratory test of a cross-flow fixed-pitch tidal  
109 turbine conducted at Newcastle University in the combined wind, wave and current tank. The  
110 experiment, a preliminary stage assessment of a larger research initiative by the University of  
111 Oxford named THAWT (Transverse Horizontal Axis Water Turbine), tested a straight bladed  
112 transverse turbine over a range of TSRs. An image of the experimental setup is shown in Fig.  
113 3.

114

115 Key features of the experimental test include;

- 116 • A three-bladed cross-flow rotor
- 117 • Aluminium disk end plates
- 118 • Belt driven power take-off coupled to a torque sensor and motor/brake
- 119 • Load cell located in a blade to directly measure radially acting force
- 120 • A NACA 0018 blade profile, circumferentially mapped such that the chord line falls  
121 on the arc of rotation of the blade
- 122 • Inclusion of a constriction to allow for the belt drive and instrumentation to be  
123 isolated from the flow

124

125 A summary of the geometric attributes of the experiment are given in Table 1. For full details  
126 of the experimental setup, calibration and error bounds, reference should be made to

127 publications by McAdam [6-8]; It should be noted that the publications present testing from  
 128 the THAWT rotor, however, the testing equipment and method are identical to the straight-  
 129 bladed variant presented in this paper.

130

| Parameter                             | Symbol | Unit | Value |
|---------------------------------------|--------|------|-------|
| Flume width                           | $b_c$  | m    | 1.8   |
| Constriction width                    | $b_r$  | m    | 1.61  |
| Flume depth                           | $h$    | m    | 1.0   |
| Height of rotor axis above flume base | $h_r$  | m    | 0.425 |
| Rotor radius                          | $r$    | m    | 0.50  |
| Blade length                          | $L_b$  | m    | 1.528 |
| Chord length                          | $c$    | mm   | 65.45 |

131

132 Table 1. Summary of experimental flume and turbine geometry

133

134 Preparation for the experimental test included using an ADCP (Acoustic Doppler Current  
 135 Profiler) to analyse the current flow at a number of pump power ratings. The profile itself,  
 136 given in Fig. 4, shows a high level of shear in the flow ranging from 0.363 m/s at the lower  
 137 boundary of the turbine to 0.275 m/s at the higher, a difference of 25%. Full turbine numerical  
 138 models of the experiment include an inlet with flow velocities that are interpolated from the  
 139 original ADV data, further details are given in section 4.1. Turbulence intensity in the  
 140 experimental flume immediately upstream of the rotor was not available, but was estimated to  
 141 be  $\approx 1\%$  (from personal correspondence with McAdam [6-8]).

142

## 143 2. Laboratory scale effects

144

145 At a nominal TSR of 3, the experimental test has an approximate  $Re$  range of 35,000 –  
 146 80,000, with the lower and higher boundaries representing rotation away from, and towards,  
 147 the incoming free stream flow respectively. This  $Re$  range is considered low for an aerofoil,  
 148 causing a highly transitional boundary layer, laminar separation, and often the formation of a

149 laminar separation bubble [9, 10]. The result is an overall poor performance in terms of lift  
150 and drag coefficients; Fig. 5 illustrates this by comparing experimental lift and drag  
151 coefficients at three progressively increasing  $Re$  for an infinite (or 2D) 0018 NACA profile  
152 blade [11, 12]. Examining Fig. 5, lift coefficient is seen to increase with  $Re$ , and stall is  
153 delayed until higher angles of attack. Similarly, the drag coefficient is higher for low  $Re$   
154 cases, decreasing and extending to higher  $\alpha$  with increasing  $Re$ . A combination of these  
155 properties results in a poorer lift to drag ratio. This issue is illustrated by McMasters [13]  
156 where an  $Re$  value of approximately  $10^5$  is identified as an average transition point for many  
157 aerofoils from a mixed boundary layer (subcritical) to one that is fully turbulent  
158 (supercritical). The boundary layer in the subcritical range, where the University of Oxford  
159 laboratory test falls, is explored experimentally by Yarusevych [14] at an  $Re$  range of 55,000  
160 – 210,000 at 0, 5 and 10 degrees  $\alpha$ . Testing with a NACA 0025, two types of boundary layer  
161 are observed; at  $Re$  values below 135,000 separations without reattachment occur, for values  
162 above, the turbulence generated in the shear layer is sufficient to promote reattachment  
163 forming a separation bubble. A variant of vortex shedding is also observed throughout the  
164 range tested, a phenomenon specific to low  $Re$  conditions that is attributed to Kelvin-  
165 Helmholtz and Tollmien-Schlichting instabilities [15, 16]. Depending on  $Re$ , these factors  
166 invariably contribute to the reduction in performance previously identified. However, the  
167 situation becomes further complicated by the effect of free stream turbulence, an issue  
168 experimentally studied by Devinant [17] for aerofoils in  $Re$  flows of 100,000 to 700,000. A  
169 superior lift and drag performance is observed as turbulence is increased due to delay of  
170 boundary separation. This behaviour is achieved numerically using Large Eddy Simulation  
171 (LES) by Kim et al. [18]. In a similar manner the surface roughness of the aerofoil can also  
172 influence the lift and drag by increasing boundary layer turbulence and thus increasing lift in  
173 subcritical flow conditions [13, 19].

174           Due to the increased flow complexity at low  $Re$ , many studies have been conducted  
175 to assess and improve the suitability of common numerical methods. The most robust of these



176 is Direct Numerical Simulation (DNS) such as that conducted by Shan et al. [20] and Alam  
177 and Sandham [21], however, the mesh densities and timestepping resolution required exclude  
178 this method from practical engineering studies [22]. Large Eddy Simulation (LES) is a less  
179 computationally expensive method and has been used by Uranga et al. [23] and Catalano &  
180 Tognaccin [24], amongst others, to successfully predict pressure and friction distributions as  
181 well as vortex instabilities. However, evidence of a superior performance over RANS  
182 methods is not explicitly established, particularly for values of lift and drag coefficient, as  
183 demonstrated by Yuan [25]. While RANS cannot offer the resolution of the previous  
184 methods, the reduced computational effort makes it the most feasible for current engineering  
185 activities. A number of publications consider various turbulence models and their suitability  
186 to capture both transition and/or lift and drag values. In particular, Windte et al. [26] and Tang  
187 [27] both attempt solutions for the SD7003, a low- $Re$  aerofoil, finding the Menter-baseline  
188 (BSL) and the Spalart-Allmaras (S-A) models superior respectively. Rumsey and Spalart [28]  
189 compare the S-A model with the Shear Stress Transport (SST) models for a NACA 0012 for  
190  $Re = 100,000$ . Both models are shown to perform similarly, displaying varying uncertainty  
191 with regard to transition onset.

192         With the SST model proving to be robust at higher  $Re$ , as shown by Eleni et al. [29]  
193 and Menter [30], adaptations to account for transition have been attempted. A prominent  
194 example for general-purpose applications is the SST  $\gamma - Re\theta$  transition model developed by  
195 Menter et al. [31]. The model adds an intermittency term,  $\gamma$ , and transition momentum  
196 thickness Reynolds number,  $Re\theta$ , to the transport equations of the SST model. The model has  
197 been empirically calibrated through experimental comparison and integrated into ANSYS  
198 CFX software as described in a paper by Menter et al. [32]. The results of validation studies  
199 by Counsil and Boulama [33] and Langtry et al. [31] show that a significant improvement is  
200 achieved over the SST in terms surface friction, and to a lesser extent the pressure distribution  
201 (due to good baseline performance). Furthermore, the computation of a T106 turbine blade at

202  $Re \approx 91,000$  by Langtry et al. [31] compares steady and unsteady application of the SST  $\gamma -$   
203  $Re\theta$  model, finding little variance between the two for pressure distribution.

204 Predictably, the more computationally intensive numerical methods, such as LES and  
205 DNS, provide increased capabilities, particularly the ability to capture the transitional  
206 boundary layers and a greater range of turbulent length scale associated with low  $Re$   
207 conditions. However, provided that heavy stall is avoided, RANS models can deliver an  
208 accurate prediction of lift and drag forces comparable with the higher resolution models. This  
209 conclusion led to the selection of a RANS methodology, with test cases being built to  
210 compare the SST and SST  $\gamma - Re\theta$  turbulence model options. It was found that the  $\gamma - Re\theta$   
211 model was particularly sensitive to  $y^+$  and did not converge well close to stall, therefore it  
212 was discounted and the standard SST model was chosen as the turbulence model for all  
213 further computational modelling.

214

### 215 **3. Isolated Blade**

216

217 The assessment of the individual blade involves the computation of a single aerofoil at angles  
218 of attack from 0-25 degrees at a flow speed such that the blade achieves a Reynolds number  
219 of 80,000. The study uses symmetrical NACA 0018 blades and a uniform inlet condition to  
220 aid validation of the lift and drag components against published data. The resultant numerical  
221 and meshing parameters are applied to the cambered blades used in the full turbine model  
222 presented in Section 4. In this study the uniform flow testing serves purely as a mesh  
223 optimisation exercise, however, research has shown that conformal mapping can be used to  
224 predict forces on cambered blades in rotational flow by modelling an equivalent profile in  
225 uniform flow [34, 35]. The numerical domain is similar to that used by Wang [36], where a  
226 rectangular far-field domain (*Fixed Domain*) with circular sub-domain (*Blade Domain*) is  
227 employed, see Fig. 6. The two domains are linked via a sliding mesh that uses a General Grid  
228 Interface (GGI) to mathematically resolve the fluxes across the interface [37]. This

229 arrangement allows the *Blade Domain* to pitch the aerofoil without re-meshing and provides a  
230 region for high grid refinement.

231

### 232 **3.1. Geometry and Boundaries**

233

234 Dimensionally, the computational domain is sufficiently large to negate blockage errors with  
235 the  $\frac{1}{4}$  chord point of the aerofoil (shown in Fig. 6) located at the centroid of both domains.

236 The boundary conditions are as follows:

237 *Inlet* – A uniform flow is specified, calculated by rearrangement of the Reynolds number for  
238 velocity  $U$ , see equation (4). Turbulence at the inlet was set by specifying an intensity  $I$  value  
239 of 1% (see section 1.2). This is converted into values of turbulence kinetic energy  $k$ ,  
240 turbulence eddy frequency  $\omega$  and turbulence dissipation  $\varepsilon$ , in the ANSYS solver using  
241 equations (7-10), where  $\mu^t$  is turbulence viscosity and  $C_\mu = 0.09$ , a non-dimensional  
242 constant.

243

$$k = \frac{3}{2} U_\infty^2 I^2 \quad (7)$$

$$\frac{\mu^t}{\mu} = 1 \quad (8)$$

$$\omega = \rho \frac{k}{\mu^t} \quad (9)$$

$$\varepsilon = C_\mu \rho \frac{k^2}{\mu^t} \quad (10)$$

244

245 *Outlet* – This is set as an ‘opening’ with a relative static pressure of zero;  $P_{rel} = 0$ .

246 *Top and bottom* – The sides assigned as ‘free-slip’ boundaries, shown in Fig. 6, allow the

247 fluid velocity component parallel to the wall to remain computed, while velocity normal to

248 the wall and the wall shear stress are set to zero;  $U_y = 0, \tau_{wall} = 0$ .

249 *Periodic faces* – All boundaries in the x-y plane are set as symmetry planes; where normal  
250 velocities and advection gradients are set to zero.

251 *Blade surfaces* – These surfaces are set to ‘no-slip’, where pressure is set to zero gradient and  
252 velocities are set to zero;  $U_x = U_y = 0$ .

253

### 254 **3.2. Meshing**

255

256 Alongside the turbulence model selection, meshing strategy is a key means of extracting the  
257 best possible outcome from the numerical model. The *Fixed Domain* contains a structured  
258 hexahedral mesh that only deforms at the interface with the *Blade Domain*. The interface was  
259 divided into 360 cells at both sides allowing for 1:1 cell alignment when the *Blade Domain* is  
260 positioned at 1 degree increments. The *Blade Domain*, shown in Fig. 7, is a mixed mesh  
261 consisting of a body fitted hexahedral mesh at the blade surface, with the remaining domain  
262 filled with wedges. Convergence studies were performed on mesh expansion ratio of the  
263 wedges (beyond the body fitted region) and the number of streamwise cells on the blade  
264 surface. The result was a low sensitivity to expansion ratio provided that the boundary layer  
265 meshing is sufficient, and that streamwise cells below the recommended aspect ratio of 100/1  
266 (width to height) showed little sensitivity provided the ratio wasn’t exceeded. The final values  
267 of 200 streamwise cells for the upper and lower blade surface, and a wedge expansion ratio of  
268 1.1, were used. This leaves the boundary layer meshing itself as the focus of the testing. In  
269 order to capture the desired accuracy of the flow at the boundary layer, as discussed in the  
270 background, the meshing is tested for maximum  $y^+$  (or  $yPlus$ ) values between 1 and 30, see  
271 equation (11), where  $\tau_\omega$  is shear stress,  $y_1$  is first layer height, and  $\nu$  is kinematic viscosity.

272

$$y^+ = \frac{\sqrt{\frac{\tau_\omega}{\rho}} \times y_1}{\nu} \quad (11)$$

273

274 **3.3. Solver control**

275

276 All models were solved using ANSYS CFX 14.0 software (under an academic license), a  
277 general purpose Navier-Stokes code. Using a steady state RANS method with a  $k-\omega$  SST  
278 turbulence model, the solutions were completed to a residual target of  $10^{-5}$  for mass and  
279 momentum terms.

280

281 **3.4. Results & Discussion**

282

283 Coefficients of lift  $C_L$  and drag  $C_D$ , given in equations (12-13), generated by the numerical  
284 models are compared in Fig. 8 alongside the result of an XFOIL V6.99 panel code simulation  
285 developed by Drela [38] and experimental data extracted from Jacobs and Sherman [11]. To  
286 correspond with the experimental turbine and numerical tests, the XFOIL solutions were  
287 computed with a free stream turbulence intensity of 1% ( $N_{crit} = 2.6224$ ). The experimental  
288 values from Jacobs and Sherman are corrected by the authors to profile values (infinite aspect  
289 ratio), with turbulence estimated to be around 0.5% - 1% for the wind tunnel used [39].

290

$$C_L = \frac{L}{\frac{1}{2}\rho U^2 c} \quad (12)$$

$$C_D = \frac{D}{\frac{1}{2}\rho U^2 c} \quad (13)$$

291

292 The experimental  $C_L$  values are closely matched by all computed  $y^+$  (written yPlus on Fig 8.)  
293 solutions up to the onset of stall at an  $\alpha$  of  $11^\circ$ , with a maximum error of  $\approx 5\%$ . The stall point  
294 is delayed by the numerical models by  $+1^\circ$  to  $2^\circ$  similar to the XFOIL result. Post-stall the  
295 SST model predicts a fluctuating lift force, as would be experienced experimentally, with flat  
296 line convergence being unachievable. These fluctuations differ with  $y^+$  with the lowest and  
297 highest values, 1 and 30 respectively, displaying the most extreme forces. In terms of drag

298 coefficient, the correlation is very similar, with pre-stall displaying high accuracy and stall  
299 being shifted up the same margin as the lift coefficient. Considering the effect of  $y^+$  on the  
300 results more closely, divergence is seen as  $\alpha$  increases for all pre-stall angles of attack.  
301 Additionally, as  $y^+$  increases,  $C_L$  is increasingly over-predicted near to stall while conversely,  
302  $C_D$  is progressively under-predicted. At a  $y^+$  of 30 the solution is beginning to diverge from  
303 the experimental values with the logarithmic wall model taking a greater part in estimating  
304 the near wall flow. In the post-stall region the highly unstable result at a  $y^+$  of 1 is due to the  
305 model attempting to resolve the viscous sublayer in full, leading to greater pressure  
306 fluctuations at the surface of the blade. Conversely, the highest  $y^+$  is excessively coarse,  
307 causing large turbulent structures to form and an unrealistically large  $C_L$  to be predicted. Mid-  
308 range  $y^+$  values offer high accuracy when predicting  $C_L$  and  $C_D$  at low  $\alpha$  and a more stable  
309 solution in post-stall conditions, therefore a  $y^+$  of 10 was chosen for all full turbine model  
310 simulations.

311 While the study gave guidance in terms of maximising the accuracy of forces at  
312 achievable angles of attack, it is expected that this range would be extended in the final model  
313 due to the effects of dynamic stall. The phenomenon is reported by Wang [36], who finds that  
314 the SST model is able to capture the delayed stall of an aerofoil in similar low  $Re$  conditions  
315 to the current study. In addition, the SST model is known to improve in accuracy with  
316 increasing  $Re$ , this was confirmed by additional numerical models built to the same  
317 constraints as those presented here.

318

#### 319 **4. Full Turbine Model**

320

321 A fully transient turbine model was developed and initially solved for TSRs between 2 and 5  
322 for comparison with the University of Oxford straight bladed turbine experimental values. To  
323 investigate scale, further solutions are generated at a TSR of 3 for turbines up to a 10 metre  
324 diameter. In order to test the robustness of possible scaling trends, additional solutions are run

325 for a TSR of 4, and for a uniform velocity profile.. Table 2 details the numerical tests  
 326 conducted, where the velocity profile is split into experimental (Exp.) or uniform flows, and  
 327  $\overline{U}_C$  and  $\overline{U}_R$  are mean velocities for the full channel depth and across the rotor respectively (see  
 328 Fig. 4.)  
 329

| Test ID | Velocity Profile | $\overline{U}_C$ (m/s) | $\overline{U}_R$ (m/s) | $\lambda$ | D (m) | $\overline{Re}$ |     |           |
|---------|------------------|------------------------|------------------------|-----------|-------|-----------------|-----|-----------|
| 1       | Exp.             | 0.333                  | 0.3698                 | 2         | 0.5   | 45,250          |     |           |
| 2       |                  |                        |                        | 2.5       |       | 55,333          |     |           |
| 3       |                  |                        |                        | 3         |       | 65,605          |     |           |
| 4       |                  |                        |                        | 3.5       |       | 75,984          |     |           |
| 5       |                  |                        |                        | 4         |       | 86,428          |     |           |
| 6       |                  |                        |                        | 4.5       |       | 96,915          |     |           |
| 7       |                  |                        |                        | 5         |       | 107,433         |     |           |
| 8       |                  |                        |                        | 3         | 0.333 | 0.3698          | 1   | 131,210   |
| 9       |                  |                        |                        |           |       |                 | 2.5 | 328,026   |
| 10      |                  |                        |                        |           |       |                 | 5   | 656,052   |
| 11      |                  |                        |                        | 4         | 0.333 | 0.3698          | 10  | 1,312,104 |
| 12      |                  |                        |                        |           |       |                 | 1   | 172,856   |
| 13      |                  |                        |                        |           |       |                 | 2.5 | 432,139   |
| 14      |                  |                        |                        |           |       |                 | 5   | 864,277   |
| 15      |                  |                        |                        |           |       |                 | 10  | 1,728,555 |
| 16      | Uniform          | 0.333                  | 0.333                  | 3         | 0.5   | 59,112          |     |           |
| 17      |                  |                        |                        |           | 1     | 118,224         |     |           |
| 18      |                  |                        |                        |           | 2.5   | 295,560         |     |           |
| 19      |                  |                        |                        |           | 5     | 591,120         |     |           |
| 20      |                  |                        |                        |           | 10    | 1,182,241       |     |           |

330  
 331 Table 2. Full turbine numerical modelling test scheme  
 332

333 Using a similar multi-domain approach to the isolated blade tests, the model consists of 3  
 334 blade domains, a rotating domain, and an outer fixed domain, as shown in Fig. 9. The  
 335 geometry represents a centre section through the  $xy$  plane of the experiment (see Fig. 6), with  
 336 turbine dimensions being identical and numerical flume height being equal to water depth.

337

#### 338 4.1. Numerical Setup

339

340 The numerical setup is based on the environment developed in the isolated blade testing in  
341 terms of boundaries, governing equations, solver convergence and meshing, with grid sizes  
342 ranging from 150,000 to 300,000 nodes. However, the simulation is now transient (unsteady  
343 RANS) with solutions running until a quasi-steady result was observed, i.e. varying with  
344 equal magnitude with each revolution. The result was considered to be converged when the  
345 average torque for 1 revolution deviated from the previous revolution by <1%, this took  
346 between 5 and 6 revolutions. Due to the implicit solution method of the software, stable  
347 convergence can be achieved at large timestep values. Therefore, timestep size was defined as  
348 the period of  $0.5^\circ$  of turbine rotation  $\theta$ , equating to courant numbers below 100 for all cases.

349 To convert the 3D experimental case into 2D, a number of assumptions were  
350 required. In particular, the effect of the experimental channel constriction is simplified into a  
351 velocity increase proportional to the decrease in area of the flume. Figure 10 illustrates this  
352 issue, where  $L_b$  is turbine blade length,  $b_T$  is test width, and  $b_C$  is channel width. Assuming  
353 water depth change is negligible through the constriction, conservation of momentum dictates  
354 that the velocity must increase equal to the ratio of area lost, i.e.  $b_C/b_T$  or 1.8/1.61. In the  
355 experimental case the rotor region (hashed area on Fig. 10) is aligned centrally within the  
356 constriction; note that the narrowing and then widening of the constriction occurs inside of  
357 the rotor's upstream and downstream extremities. The position of these constriction changes,  
358 and hence velocity, are problematic for the 2D model, therefore it is assumed that the whole  
359 turbine is subject to the velocity increase and that TSR is maintained for the upstream half of  
360 the rotor, i.e. rotational velocity is calculated from the increased mean inlet velocity. The final  
361 inlet of the numerical tank took the form of a depth based interpolation of the original  
362 velocity profile (see Fig. 4) multiplied by the area ratio 1.8/1.61. It was confirmed that the  
363 numerical model succeeded in propagating the velocity profile from the inlet to the rotor with  
364 minimal change.

365 Having already made the assumption that depth change is negligible, the model also  
366 excludes a free surface, instead using a 'free slip' condition at the upper boundary. These



367 simplifications have been previously shown to have little effect on the numerical result for  
368 overall turbine torque, see [40].

369

## 370 **4.2 Results & Discussion**

371

372 The experimental data was collected by gradual ramping of the turbine rotation from zero up  
373 to a TSR of 5 and back to zero during which torque and force sensors recorded the turbine's  
374 responses. Due to the cyclic delivery of the torque, the collected data was smoothed using  
375 resampling (see McAdam [6]), from which values of power coefficient  $C_P$ , torque  $C_Q$  and  
376 thrust  $C_T$  were calculated. The ramping experimental methodology produced a slight  
377 variation in the results between the rising and falling data due to the reaction time of the  
378 motor/brake; therefore an average of the two has been taken to produce the final values. A  
379 similar mean is calculated for torque  $Q$  and thrust  $T$  from the numerical result by averaging  
380 each value over a single  $360^\circ$  rotation of the turbine, where power  $P = Q\lambda$ , and thrust is the  
381 force equal and opposite to the streamwise drag of the entire rotor. Simulations were  
382 computed on the University of Bath 'Aquila' high performance computer taking an average of  
383 48 hours on 4 processors to complete. All values of  $C_P$ ,  $C_Q$  and  $C_T$  are based upon the  
384 available kinetic energy within the limits of the rotor (see Fig. 4), using equations (14), (15)  
385 and (16) respectively, where  $A$  is the swept area of the rotor seen by the flow, and  $U_r$  is the  
386 mean flow velocity within rotor area  $A$ .

387

$$C_P = \frac{P}{\frac{1}{2}\rho A U_r^3} \quad 14$$

$$C_Q = \frac{C_P}{\lambda} \quad 15$$

$$C_T = \frac{T}{\frac{1}{2}\rho A U_r^2} \quad 16$$

388

389 **4.2 .1 Lab Scale**

390

391 All three parameters given in equations (14-16) are plotted in Fig. 11 for experimental and  
392 numerical methods. Comparing the two results for  $C_P$  shown in Fig. 11 (a), it is clear that the  
393 numerical model achieves high correlation with the experiment. At close inspection the  
394 numerical result slightly under predicts  $C_P$  below a TSR of 3, changing to over prediction by a  
395 maximum of  $\approx 10\%$  at a TSR of 4. Qualitatively the numerical result matches the experimental  
396 values, showing a rising value of  $C_P$  up to a TSR of 4, before losing efficiency and falling as  
397 TSR rises to 5. Identical trends for both torque coefficient plotted in Fig. 11 (b), and thrust  
398 coefficient in Fig. 11 (c), where the crossing points between numerical and experimental  
399 values also fall at a TSR of 3, with peak torque falling at the lower TSR of  $\sim 3.6$  as would be  
400 expected.

401 The quantitative error of the numerical model can be attributed to a number of  
402 limitations. At low TSR the reduced accuracy and marginal under-prediction of forces of the  
403 SST model at post-stall angles of attack, as shown in Fig. 8, would explain the lower than  
404 expected values. Above a TSR of 3, the over prediction is more significantly influenced by  
405 the required simplification of the 3D constriction of the flume into a 2D model. To achieve  
406 this the correction requires an increased angular velocity employed in the numerical model to  
407 maintain TSR with the corrected inlet velocity, as detailed in section 4.1, and therefore may  
408 result in the over prediction of turbine performance.

409 Despite the limitations imposed by the low  $Re$  conditions, the simplified numerical  
410 model has accurately predicted trends and quantitative values within a peak error of  $\pm 10\%$  for  
411 all coefficients. It is worth noting that all numerical results fall into the extremities of the  
412 experimental raw data (example shown in McAdam [6]), with the experiment itself being  
413 subject to range of instrumentation and experimental error tolerances.

414 To explore the accuracy of the simulation further, Fig. 12 shows the coefficient of  
415 distributed normal load  $C_N$ , given in equation (17), for experimental and numerical results for

416 TSRs of 2, 3 and 4; where  $N$  is the distributed normal load. For clarity, the load given is  
417 acting radially, where positive values are acting away from the turbine axis (see [7]).

418

$$C_N = \frac{N}{\frac{1}{2}\rho c U_r^2} \quad 17$$

419

420 Considering the slowest spinning turbine case, at a TSR of 2, Fig. 12 (a) shows that the  
421 numerical simulation achieves broad correlation with experiment, but with diverging force  
422 oscillations visible in the 180-360 degree region. Referring to Fig. 1, at rotation angles  
423 ( $\theta$ ) below 180 degrees the blades are upstream, and above 180 degrees they are downstream.  
424 In the downstream region, due to the low TSR and velocity shadow induced by the upstream  
425 wake, the blades experience the lowest blade chord Reynolds numbers modelled in this  
426 research, resulting in heavy stall of the downstream blades. In such conditions the unsteady  
427 RANS method is unable to accurately resolve the flow shear around the blades resulting in a  
428 poor match in this region.

429 At a TSR of 3, Fig. 12 (b) shows an improved correlation with the experimental  
430 readings compared to Fig. 12 (a). The positives include a qualitatively high match, with  
431 almost all of the peaks and troughs captured by the numerical model. In particular, the  
432 downstream values suggest that the generation and advection of shear flows is taking place  
433 with consummate accuracy. The origins of the load force fluctuations are highlighted in Fig.  
434 13 which presents a contour plot of the flow field velocities for the same numerical result.  
435 The velocities have been limited to values from 0.125 to 0.625 in order to visually capture the  
436 advection of velocity fluctuations generated by the upstream blade wake. By comparing Fig.  
437 12 (b) and Fig. 13 it is possible to correlate the fluctuations in force between  $\theta$  positions of  
438 170° and 250° to the dynamic vortex shedding shown in the contour plot. Similarly, the wake  
439 fluctuations passing the downstream blade between the 270° and 350° positions are also  
440 visible in both the force prediction and the contour plot. Quantitatively the zero degree value  
441 and the downstream values are below expected. Causes include possible free surface effects

442 for values close to zero degrees and the inability of the 2D model to capture the effect of the  
443 diverging flume side walls as shown in Fig. 10.

444         Increasing the speed of the turbine to a TSR of 4, Fig. 12 (c) shows similar attributes  
445 to those in Fig. 12 (b). The upstream quantitative values are particularly well matched with  
446 the extreme loading predicted within 5% of the experimental value. Downstream the result  
447 diverges more significantly from experimental values and appears as a smoother line.

448         The reduced forces numerically predicted at the downstream positions for TSRs of 3  
449 and 4 suggest that there is unexpected loss in flow velocity between upstream and  
450 downstream locations. Along with the issues raised already in the discussion, this discrepancy  
451 may also be a symptom of a higher free stream turbulence than was estimated for the  
452 experiment, causing faster wake recovery. Additionally, the influence of the velocity  
453 correction to account for the constriction may result in an increased blade efficiency at the  
454 upstream position and hence result in a lower flow speed downstream. It should be noted that  
455 the experimental plot is an instantaneous result, demonstrated by the  $0^\circ$  and  $360^\circ$  differing in  
456 Fig. 12 (a-c), and therefore is subject to variances which may not reflect the exact average of  
457 the force acting on the turbine blade.

458

#### 459 **4.2.2 Turbine Scaling**

460

461 To explore the effect of Reynolds number scaling on turbine performance a series of  
462 simulations were performed at turbine diameters of 0.5m, 1m, 2.5m, 5m and 10m, with 0.5m  
463 being the lab scale model. Each test includes a velocity profile equivalent to the lab scale inlet  
464 that has stretched depth-wise such that the overall resolved flow velocities and directions  
465 experienced by the blade are equal at all scales. The study includes three sets of results (S1,  
466 S2 and S3), referring to Table 2, S1 comprises of tests 3, 8-11, S2 from 5, 12-15, and S3 from  
467 tests 16-20. The three sets represent three alternative turbine operating conditions, TSR 3 and  
468 TSR 4 in the experimental velocity profile, and TSR 3 in uniform flow conditions.

469           The results for the scaling tests are shown in Fig. 14, where all results are plotted  
470 against  $\overline{Re}$ . Starting with the Coefficient of power in Fig. 14 (a), the three scaling tests are  
471 plotted with each marker representing a result at each increment of geometric scaling; the  
472 result for test set S1 is labelled as an example. A number of significant findings can be  
473 observed, firstly, the power coefficient increases significantly from low  $\overline{Re}$ , lab scale  
474 conditions, up to the full scale equivalent. For example, S1 increases by over 200% from the  
475 experimental lab scale, for a rotor experiencing a mean blade chord Reynolds number 20  
476 times higher. Secondly, the rate of increase is non-linear, with all three test cases displaying a  
477 decaying increase in  $C_p$ . Additionally, the three test cases show little correlation with each  
478 other. For example, at low  $\overline{Re}$ , equivalent to lab scale, S2 gives the highest  $C_p$ , S3 medium  
479 value, and S1 the lowest. At high  $\overline{Re}$  values of  $>10^6$ , equivalent to a full scale turbine, the  
480 order of performance is altered such that S3 provides the highest  $C_p$ , S1 medium, and S2 the  
481 lowest performing turbine. However, at an  $\overline{Re}$  of approximately 350,000 the power  
482 coefficients of all three cases rise with equal gradients signifying that the effects of low  $\overline{Re}$   
483 conditions are diminishing, with the solution converging towards an asymptote.

484           Fig. 14 (b) shows the change in torque coefficient with  $\overline{Re}$ , where  $C_Q$  is non-  
485 dimensionalised by equation (15). Unlike the plot for  $C_p$  the three test results do not cross,  
486 but display an otherwise equivalent behaviour.

487           The final plot, Fig. 14 (c), shows thrust coefficient against  $\overline{Re}$ . All three sets  
488 experience a lower relative thrust at lab scale than would be expected at full scale. In parallel  
489 to the  $C_p$ , the thrust becomes increasingly constant at an  $\overline{Re}$  of  $\sim 350,000$  and above.

490

## 491 **5. Conclusions**

492

493           An experimental test conducted by the University of Oxford has been used as a basis to  
494 develop and validate a numerical model of a three bladed variant of a cross-flow turbine. The

495 resultant model has been adapted to explore performance at increased scales and identify  
496 relationships and limitations in both the experimental and numerical methods.

497 An isolated blade case was used to classify and validate prediction of lift and drag  
498 coefficients using a RANS numerical model employing the  $k - \omega$  SST turbulence model.  
499 The result showed a high degree of correlation with experimental values for all angles of  
500 attack below stall, with a maximum error in lift coefficient  $\approx 5\%$ . In post-stall conditions  
501 stability of the numerical solution proved to be sensitive to  $y^+$  with values between 10 and 15  
502 found to be the most stable. This range falls directly in the transition region, defined as 11.06  
503 for  $\omega$  based models, between the linear near wall layer and the logarithmic region of the  
504 boundary layer.

505 The results of the numerical modelling of the University of Oxford laboratory scale  
506 turbine confirm that a URANS methodology with 2D simplification is capable of providing  
507 accurate hydrodynamic performance predictions for cross-flow turbines. For all practical  
508 turbine operation speeds the maximum quantitative error for  $C_p$  was 8%, with positive  
509 qualitative agreement achieved for all variables (see Fig. 11). Investigating local forces on the  
510 blades showed that the numerical model is capturing not only global averages, but also  
511 advecting realistic turbulent structures through the turbine in cases where deep stall is  
512 avoided. The most prominent example of this is shown in Fig. 12 (b), supported by Fig. 13,  
513 where the numerical results capture the downstream fluctuation of  $C_N$  due to the generated  
514 upstream wake in parallel with the experiment. Limitations to the numerical accuracy of the  
515 lab scale result include the negation of the flume narrows, velocity correction and turbulence  
516 assumptions, and very low  $Re$   $\omega$  equation performance in the boundary layer.

517 Scaling of the turbine was approached by focussing on the changes to device  
518 performance with mean blade chord Reynolds number  $\overline{Re}$ . Based on the high validation  
519 achieved at lab scale, and the known improvement to blade force prediction using  $\omega$  based  
520 models at increased Reynolds numbers, a purely numerical series of tests were conducted.  
521 The scaling tests, detailed in Table 2, generated a number of findings including:

522

- 523 • At full scale/high  $Re$  the turbine achieves significantly higher power coefficients than  
524 an equivalent lab scale model
- 525 • The increase in power coefficient with scale is non-linear and varies inconsistently  
526 between operating conditions for values of  $\overline{Re}$  below  $\sim 350,000$ .
- 527 • Above an  $\overline{Re}$  of  $\sim 350,000$ , the power coefficients of all operating conditions become  
528 equally proportional.

529

530 The rise in  $C_p$  at higher Reynolds numbers is expected and supports existing  
531 literature. However, the inconsistency of the increase in  $C_p$  between the three operating  
532 conditions shown in Fig. 14 shows conclusively that tests both numerically or experimentally  
533 do not scale consistently when referenced against mean Reynolds number. For example, Set  
534 2, TSR 4 – experimental flow, was the highest performing of all three cases, but by an  $\overline{Re}$   
535  $\sim 250,000$  this had fallen to the worst performing. The transition between varying and  
536 proportional results falling at  $\sim 350,000$  is consistent with the boundary layer transformation  
537 of the selected foil from a mixed to a supercritical boundary layer, this change is key to the  
538 behaviour demonstrated in the results. Additionally, the boundary layer behaviour has the  
539 knock-on effect of triggering dynamic stall with leading and trailing edge vortex generation  
540 causing turbulent structures that have a non-trivial effect on upstream and downstream blade  
541 performance. For these reasons, the results advocate the use of a minimum  $\overline{Re}$  of  $\sim 350,000$   
542 for laboratory scale tests in order to avoid low  $Re$  effects and provide scalability and  
543 proportionality to the acquired turbine performance data. Furthermore, the reduction in  
544 uncertainty may also improve the isolation and application of additional corrections such as  
545 accounting for Froude number and blockage. For alternative turbine geometries differing  $\overline{Re}$   
546 limits are likely to exist and therefore should be considered alongside other known effects  
547 when inferring full scale turbine performance from low  $Re$  test data.

548

549 **6. Acknowledgements**

550

551 Ross McAdam and Guy Houlsby of the University of Oxford are thanked for providing the  
552 experimental data used in this study for validation of the numerical simulations.

553



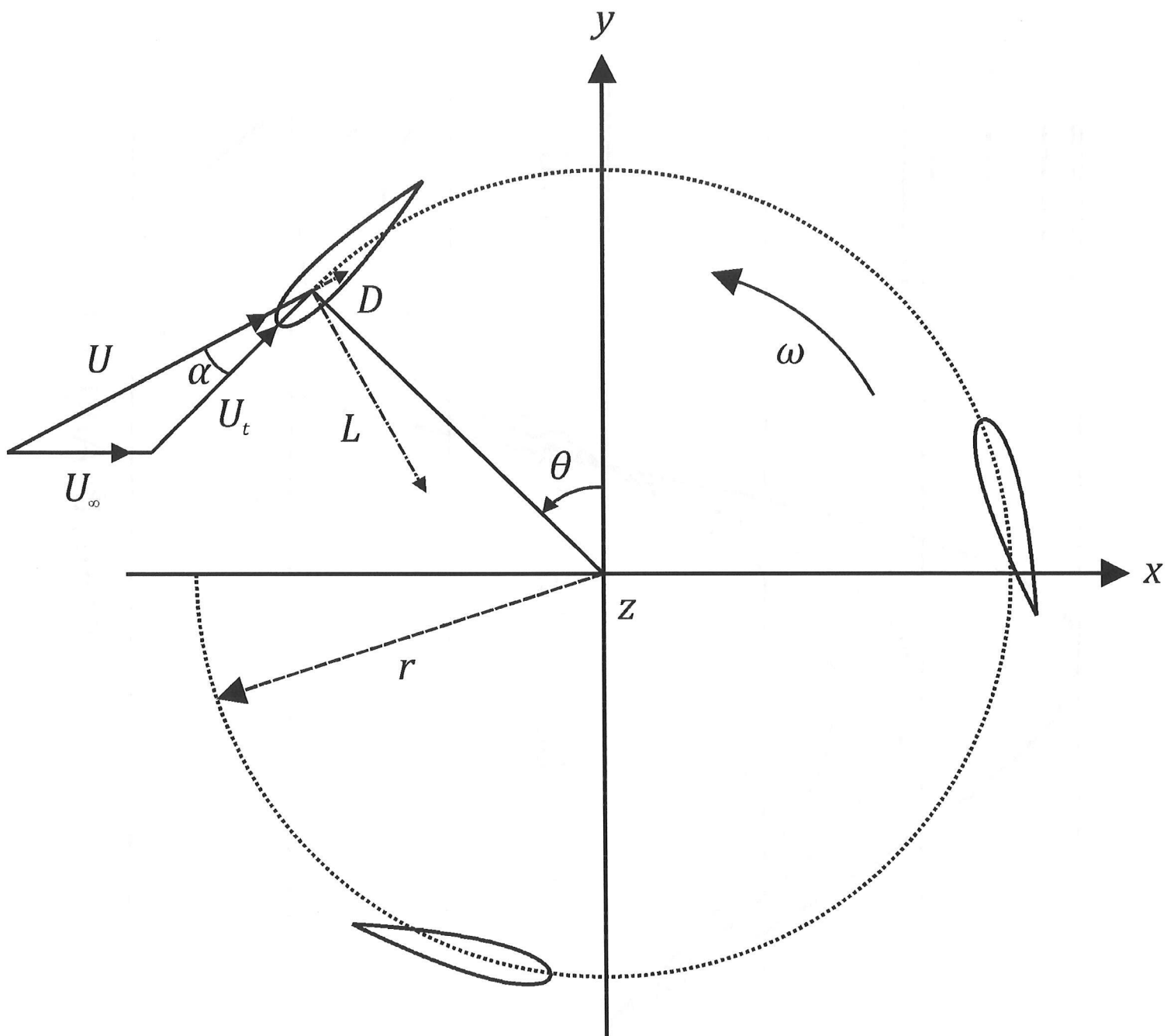
554 **References**

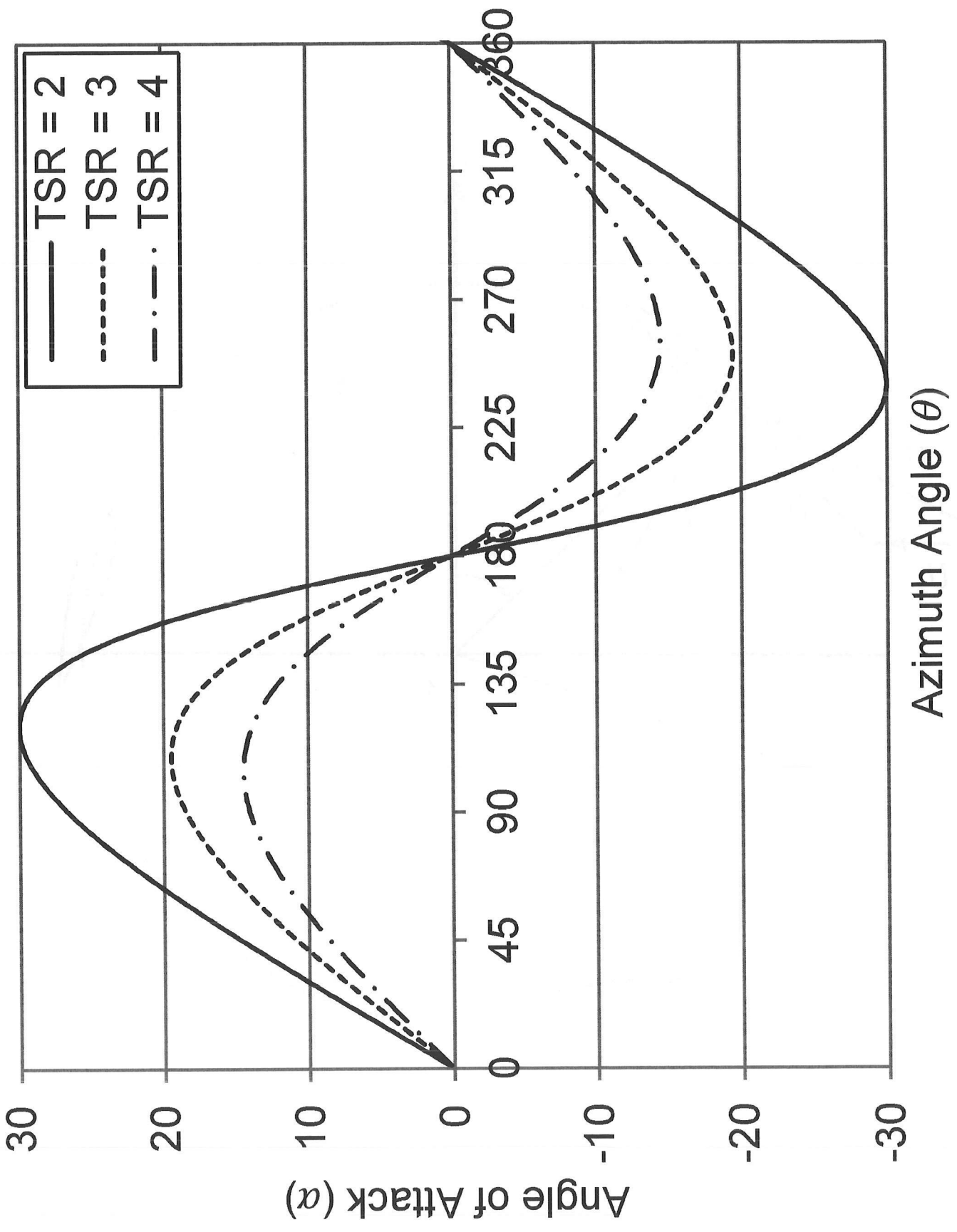
555

- 556 1. University of Oxford. Tidal Energy Research Group. Available from:  
557 <http://www.eng.ox.ac.uk/tidal/research/thawt>.
- 558 2. Calcagno, G., et al., *Experimental and numerical investigation of an*  
559 *innovative technology for marine current exploitation: the Kobold turbine.*  
560 Proceedings of the Sixteenth (2006) International Offshore and Polar  
561 Engineering Conference, Vol 1, 2006: p. 323-330.
- 562 3. Darrieus, G.J.M., *Turbine having its rotating shaft transverse to the flow of the*  
563 *current*, U.S.P. Office, Editor. 1931.
- 564 4. Lynn, P.A.a., *Electricity from wave and tide : an introduction to marine*  
565 *energy.*
- 566 5. Whelan, J. and T. Stallard. *Arguments for modifying the geometry of a scale*  
567 *model rotor.* in *9th European Wave and Tidal Energy Conference*  
568 *(EWTEC2011).* Southampton.
- 569 6. McAdam, R.A., G.T. Houlby, and M.L.G. Oldfield, *Experimental*  
570 *measurements of the hydrodynamic performance and structural loading of the*  
571 *Transverse Horizontal Axis Water Turbine: Part 1.* Renewable Energy, 2013.  
572 **59**(0): p. 105-114.
- 573 7. McAdam, R.A., G.T. Houlby, and M.L.G. Oldfield, *Experimental*  
574 *measurements of the hydrodynamic performance and structural loading of the*  
575 *Transverse Horizontal Axis Water Turbine: Part 2.* Renewable Energy, 2013.  
576 **59**: p. 141-149.
- 577 8. McAdam, R.A., G.T. Houlby, and M.L.G. Oldfield, *Experimental*  
578 *measurements of the hydrodynamic performance and structural loading of the*  
579 *Transverse Horizontal Axis Water Turbine: Part 3.* Renewable Energy, 2013.  
580 **59**: p. 82-91.
- 581 9. Hain, R., C.J. Kahler, and R. Radespiel, *Dynamics of laminar separation*  
582 *bubbles at low-Reynolds-number aerofoils.* Journal of Fluid Mechanics, 2009.  
583 **630**: p. 129-153.
- 584 10. Selig, M.S., et al., *Experiments on Airfoils at Low Reynolds Numbers.* AIAA  
585 Paper 96-0062, 1996.
- 586 11. Jacobs, E.N. and A. Sherman, *Airfoil Section Characteristics as Affected by*  
587 *Variations of the Reynolds Number.* NACA Report no. 586, 1937.
- 588 12. Jacobs, E.N., K.E. Ward, and R.M. Pinkerton, *The characteristics of 78*  
589 *related airfoil sections from tests in the variable-density wind tunnel.* NACA  
590 Report 460, 1933.
- 591 13. McMasters, J.H. and M.L. Henderson, *Low-Speed Single Element Airfoil*  
592 *Synthesis.* Technical Soaring, 1979. **4**(2): p. 1-21.
- 593 14. Yarusyevych, S., P.E. Sullivan, and J.G. Kawall, *On vortex shedding from an*  
594 *airfoil in low-Reynolds-number flows.* Journal of Fluid Mechanics, 2009. **632**:  
595 p. 245-271.
- 596 15. Lin, J.C.M. and L.L. Pauley, *Low-Reynolds-number separation on an airfoil.*  
597 Aiaa Journal, 1996. **34**(8): p. 1570-1577.
- 598 16. Brinkerhoff, J.R. and M.I. Yaras, *Interaction of viscous and inviscid instability*  
599 *modes in separation-bubble transition.* Physics of Fluids, 2011. **23**(12).

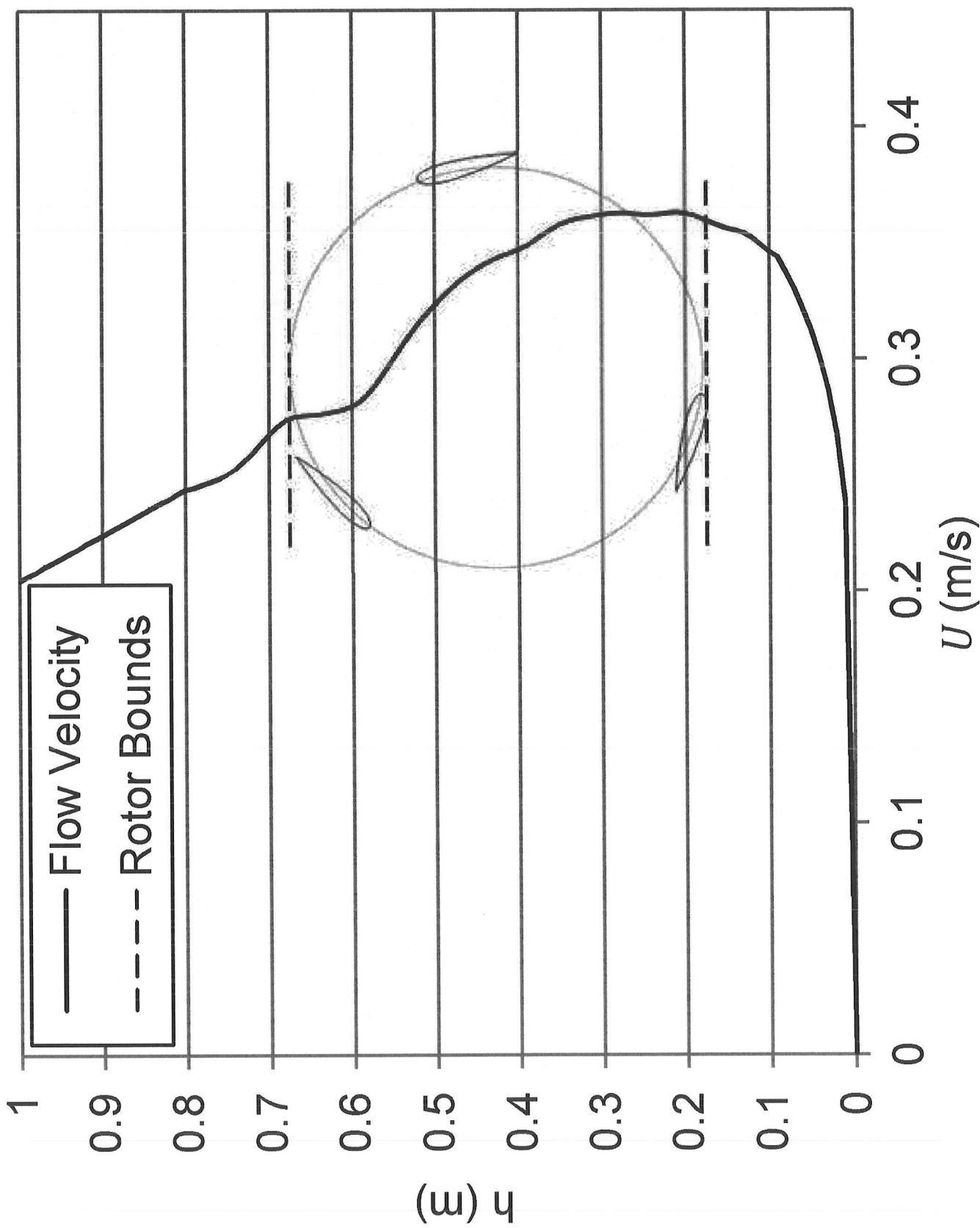
- 600 17. Devinant, P., T. Laverne, and J. Hureau, *Experimental study of wind-turbine*  
601 *airfoil aerodynamics in high turbulence*. Journal of Wind Engineering and  
602 Industrial Aerodynamics, 2002. **90**(6): p. 689-707.
- 603 18. Kim, Y., Z.T. Xie, and I.P. Castro *LES study of a wind turbine airfoil flow in*  
604 *turbulence*.
- 605 19. Santhanakrishnan, A., et al., *Enabling Flow Control Technology for Low*  
606 *Speed UAVs*. 2005.
- 607 20. Shan, H., L. Jiang, and C.Q. Liu, *Direct numerical simulation of flow*  
608 *separation around a NACA 0012 airfoil*. Computers & Fluids, 2005. **34**(9): p.  
609 1096-1114.
- 610 21. Alam, M. and N.D. Sandham, *Direct numerical simulation of 'short' laminar*  
611 *separation bubbles with turbulent reattachment*. Journal of Fluid Mechanics,  
612 2000. **410**: p. 1-28.
- 613 22. Coleman, G.N. and R.D. Sandberg, *A Primer on direct numerical simulation*  
614 *of turbulence - methods, procedures and guidelines.*, in *Tech. Rep AFM-*  
615 *09/01a*. 2010, Aerodynamics & Flight Mechanics Research Group, School of  
616 Engineering Sciences. University of Southampton.
- 617 23. Uranga Cabrera, A., *Investigation of transition to turbulence at low Reynolds*  
618 *numbers using Implicit Large Eddy Simulations with a Discontinuous*  
619 *Galerkin method*. 2010, Massachusetts Institute of Technology. p. 164 p.
- 620 24. Catalano, P. and R. Tognaccini, *Large Eddy Simulations of the Flow around*  
621 *the SD 7003 Airfoil*, in *AIMETA Conference 2011*. 2011: Bologna.
- 622 25. Yuan, W., et al., *A parametric study of LES on laminar-turbulent transitional*  
623 *flows past an airfoil*. International Journal of Computational Fluid Dynamics,  
624 2006. **20**(1): p. 45-54.
- 625 26. Windte, J., U. Scholz, and R. Radespiel, *Validation of the RANS-simulation of*  
626 *laminar separation bubbles on airfoils*. Aerospace Science and Technology,  
627 2006. **10**(6): p. 484-494.
- 628 27. Tang, L., *Reynolds-averaged Navier-Stokes simulation of low-Reynolds-*  
629 *number airfoil aerodynamics*. Journal of Aircraft, 2008. **45**(3): p. 848-856.
- 630 28. Rumsey, C.L. and P.R. Spalart, *Turbulence Model Behavior in Low Reynolds*  
631 *Number Regions of Aerodynamic Flowfields*. Aiaa Journal, 2009. **47**(4): p.  
632 982-993.
- 633 29. Eleni, D.C., T.I. Athanasios, and M.P. Dionissios, *Evaluation of the*  
634 *turbulence models for the simulation of the flow over a National Advisory*  
635 *Committee for Aeronautics (NACA) 0012 airfoil*.
- 636 30. Menter, F.R., *2-Equation Eddy-Viscosity Turbulence Models for Engineering*  
637 *Applications*. Aiaa Journal, 1994. **32**(8): p. 1598-1605.
- 638 31. Menter, F.R., R. Langtry, and S. Volker, *Transition modelling for general*  
639 *purpose CFD codes*. Flow Turbulence and Combustion, 2006. **77**(1-4): p. 277-  
640 303.
- 641 32. Menter, F.R., et al., *A correlation-based transition model using local variables*  
642 *- Part I: Model formulation*. Journal of Turbomachinery-Transactions of the  
643 Asme, 2006. **128**(3): p. 413-422.
- 644 33. Counsil, J.N.N. and K.G. Boulama, *Validating the URANS shear stress*  
645 *transport gamma - Re-theta model for low-Reynolds-number external*  
646 *aerodynamics*. International Journal for Numerical Methods in Fluids, 2012.  
647 **69**(8): p. 1411-1432.

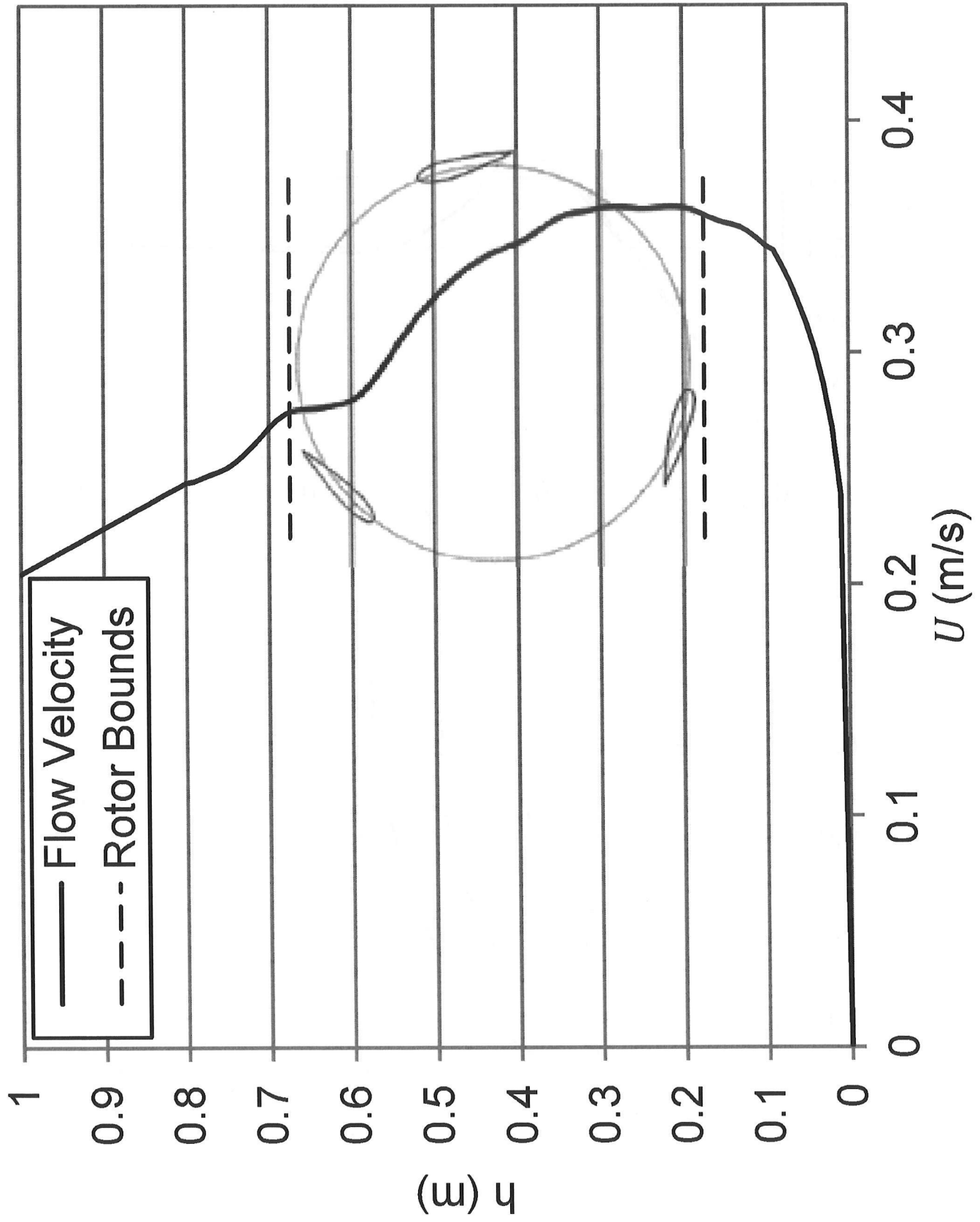
- 648 34. Migliore, P.G., W.P. Wolfe, and J.B. Fanucci, *Flow Curvature Effects on*  
649 *Darrieus Turbine Blade Aerodynamics*. Journal of Energy, 1980. 4(2): p. 49-  
650 55.
- 651 35. Hiromichi, A., et al., *A conformal mapping technique to correlate the rotating*  
652 *flow around a wing section of vertical axis wind turbine and an equivalent*  
653 *linear flow around a static wing*. Environmental Research Letters, 2013. 8(4):  
654 p. 044040.
- 655 36. Wang, S.Y., et al., *Numerical investigations on dynamic stall of low Reynolds*  
656 *number flow around oscillating airfoils*. Computers & Fluids, 2010. 39(9): p.  
657 1529-1541.
- 658 37. Galpin, P.F., R.B. Broberg, and B.R. Hutchinson, *Three-dimensional Navier-*  
659 *Stokes Predictions of Steady State Rotor/Stator Interaction with Pitch Change*,  
660 *in Third Annual Conference of CFD Society of Canada*. 1995: Banf, Ontario,  
661 Canada.
- 662 38. Drela, M., *XFOIL: An analysis and design system for low Reynolds number*  
663 *airfoils*, in *Low Reynolds number aerodynamics*. 1989, Springer. p. 1-12.
- 664 39. Dryden, H.L.A., Ira H, *The design of low-turbulence wind tunnels*. National  
665 Advisory Committee for Aeronautics, 1948(Technical Note No. 1755).
- 666 40. C.A.Consul, R.H.J.W. *An Investigation of the Influence of Free Surface*  
667 *Effects on the Hydrodynamic Performance of Marine Cross-Flow Turbines*. in  
668 *9th European Wave and Tidal Energy Conference*. 2011. Southampton, UK.  
669



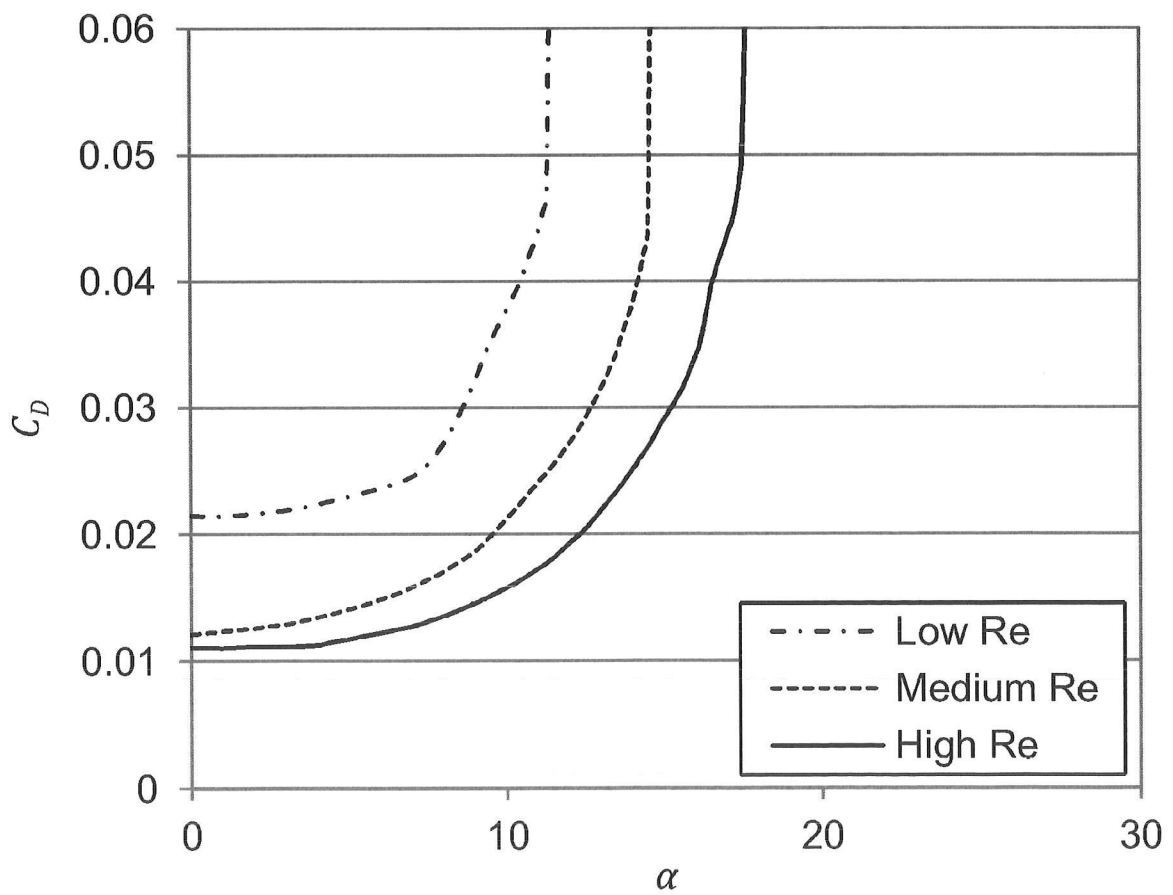
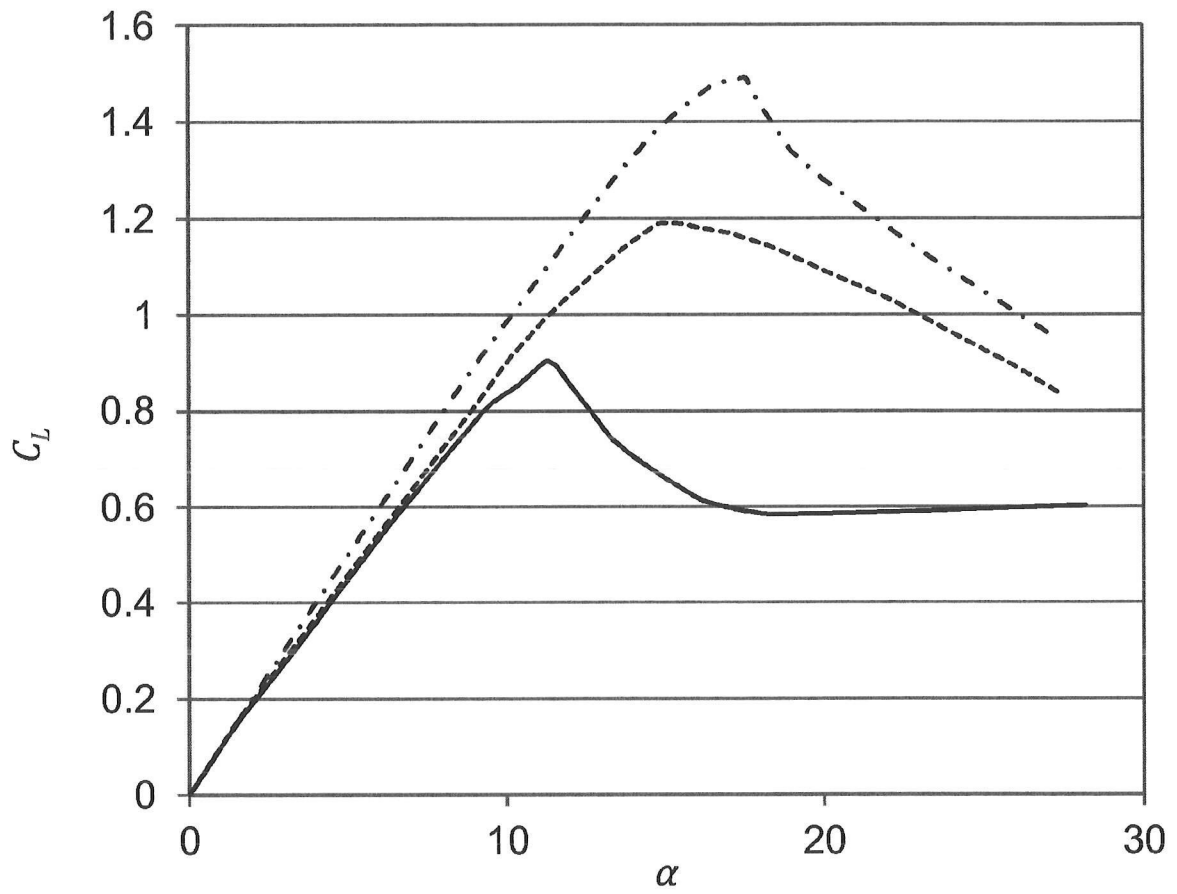


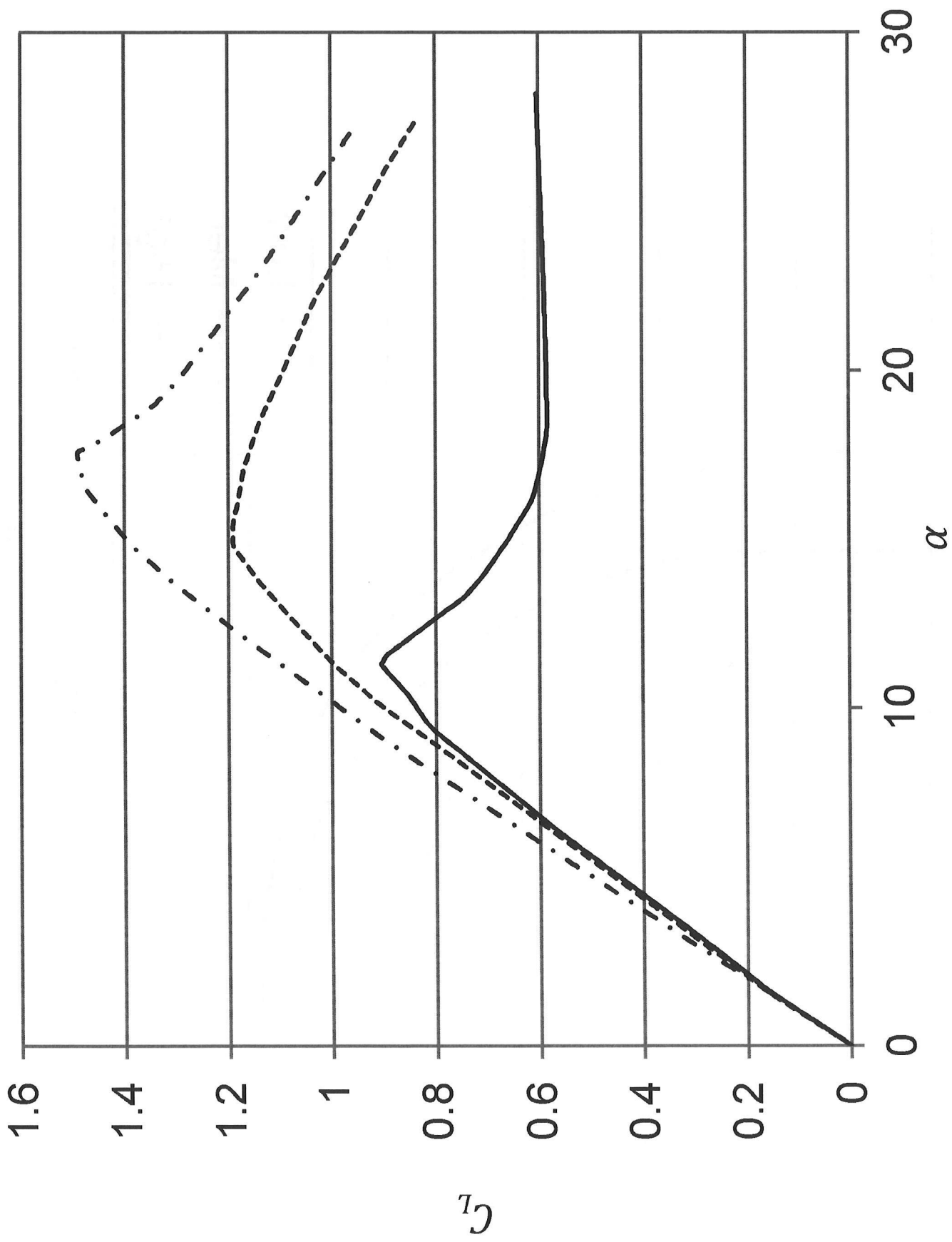


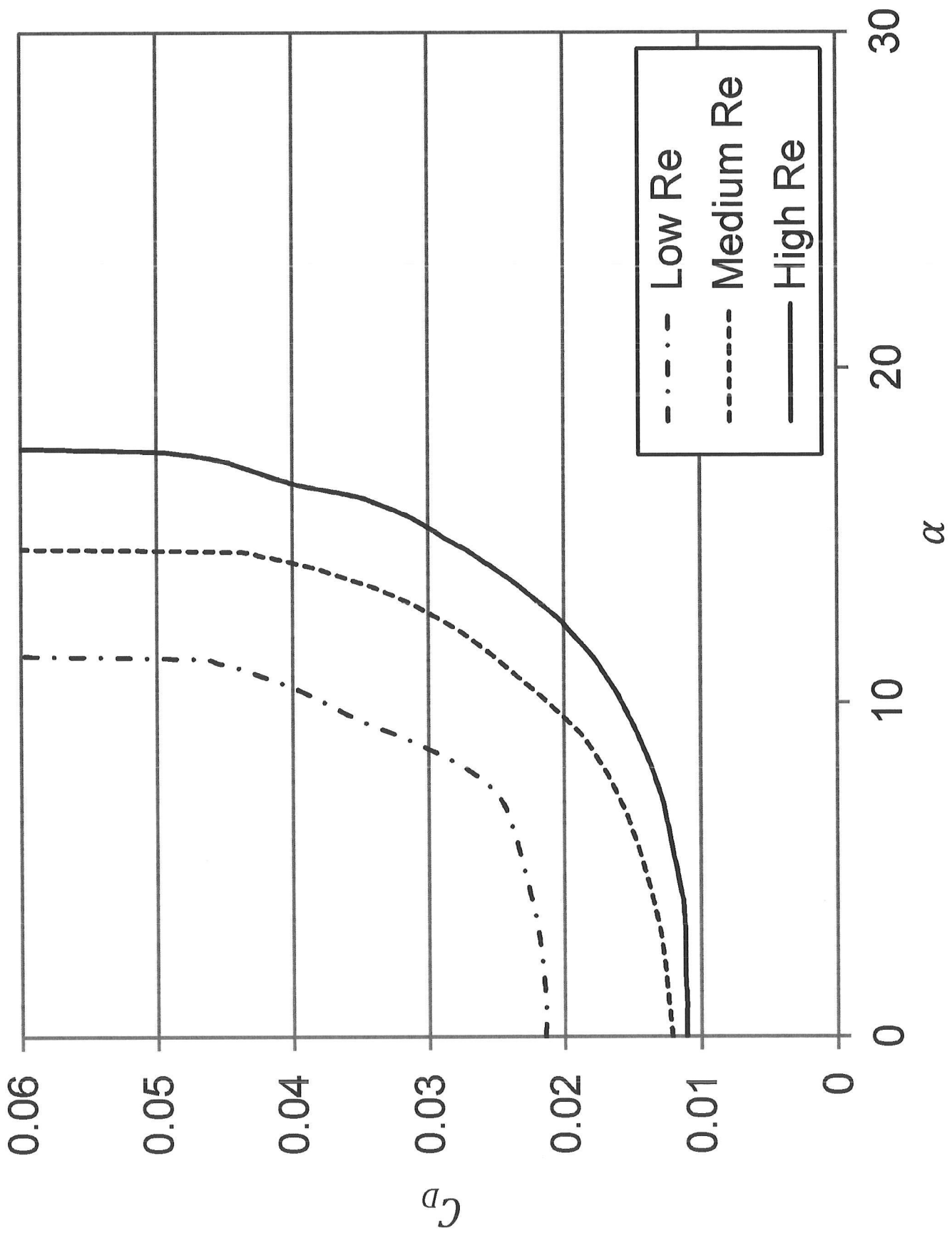


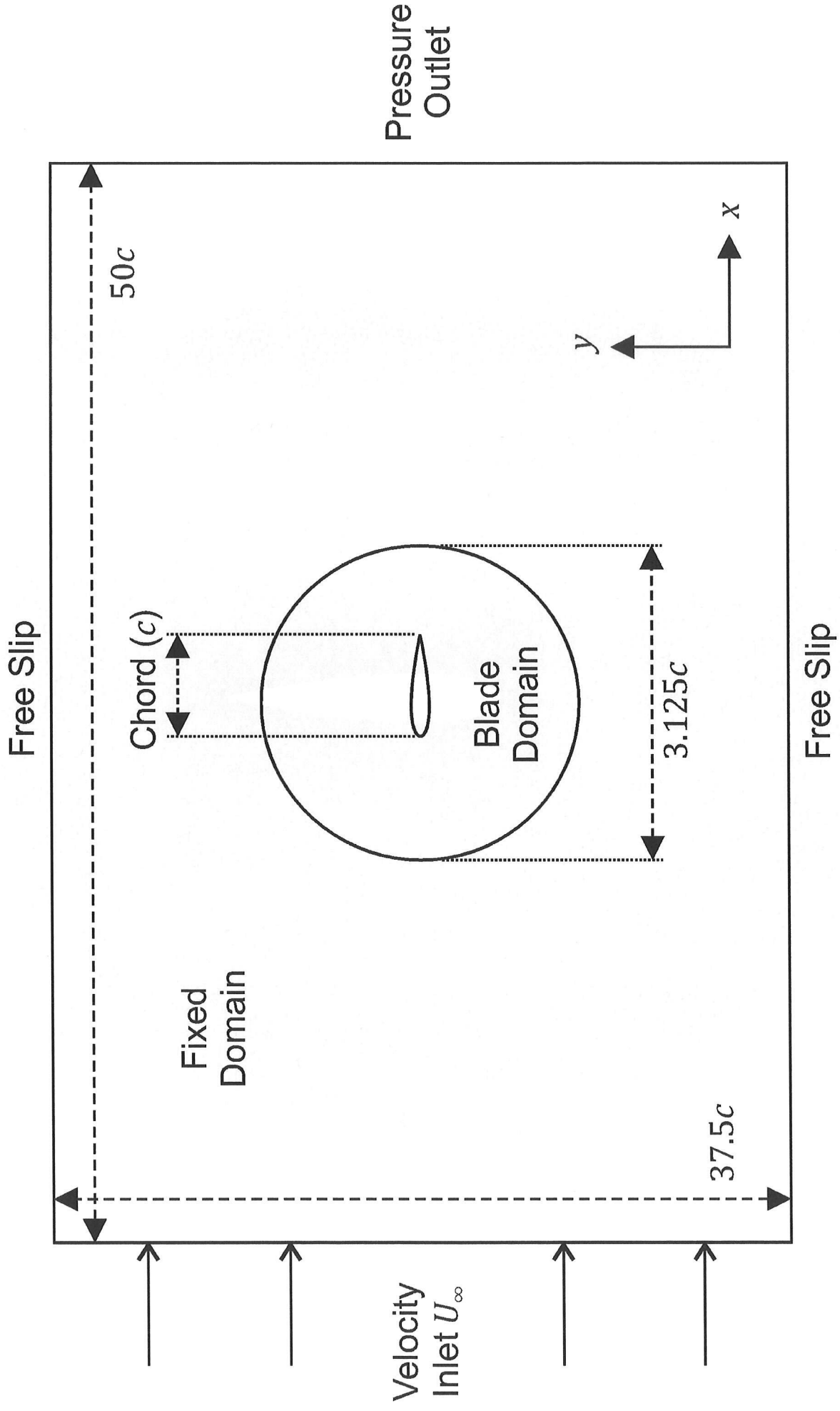


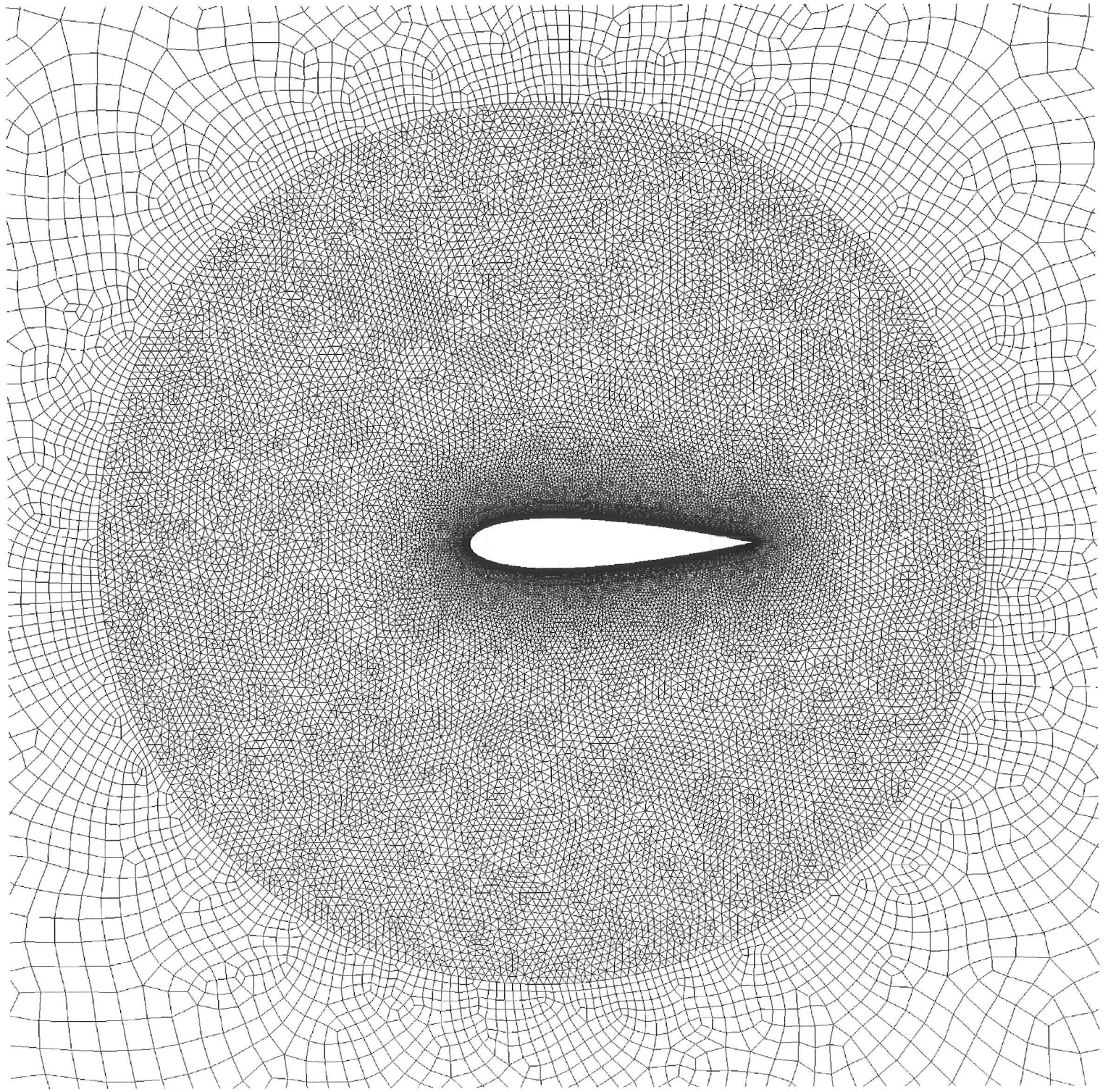


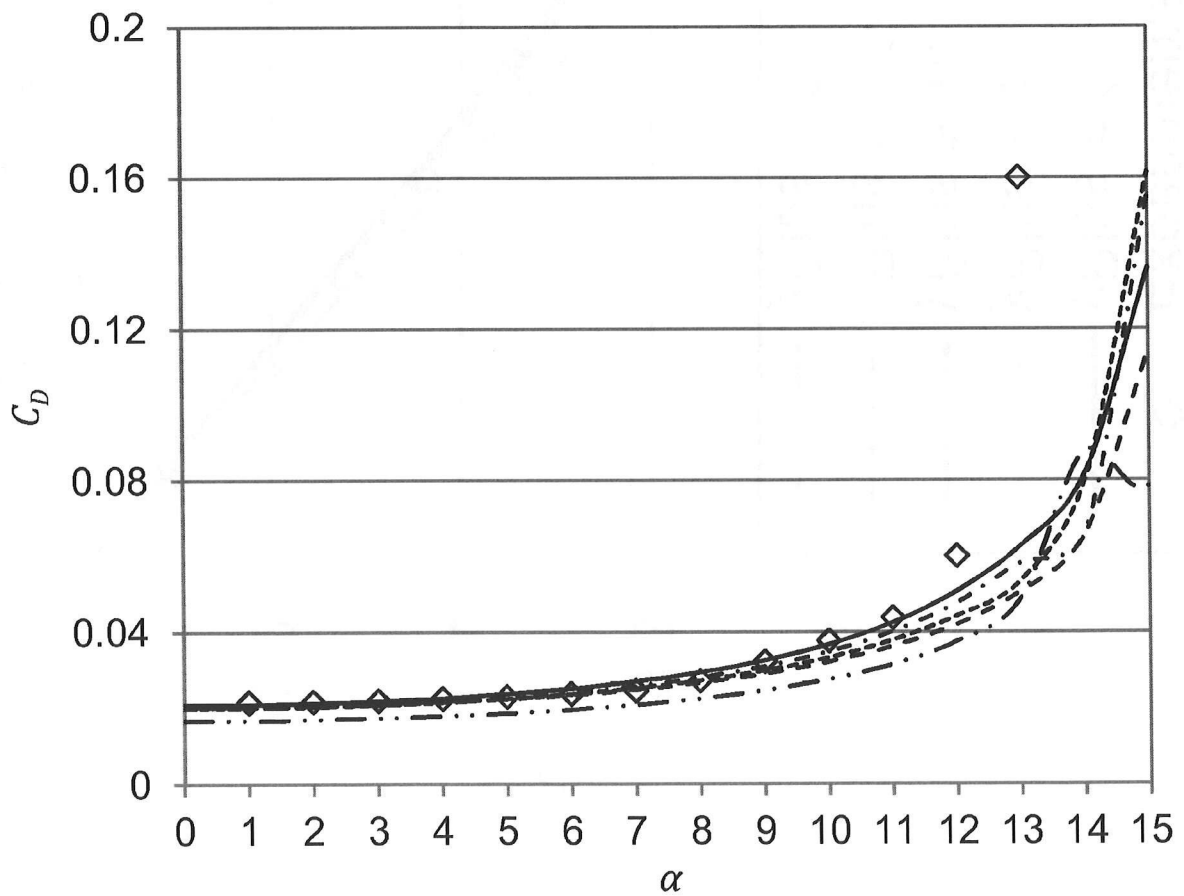
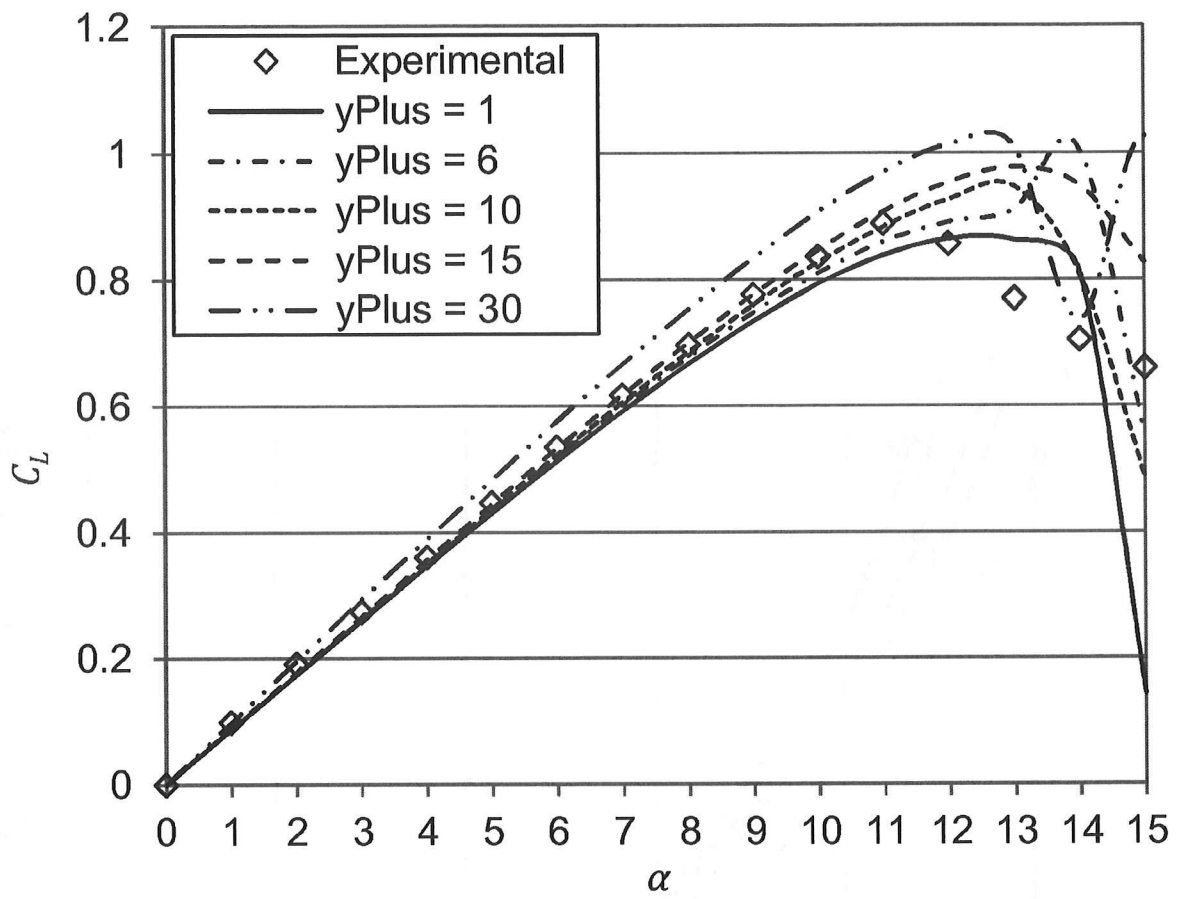


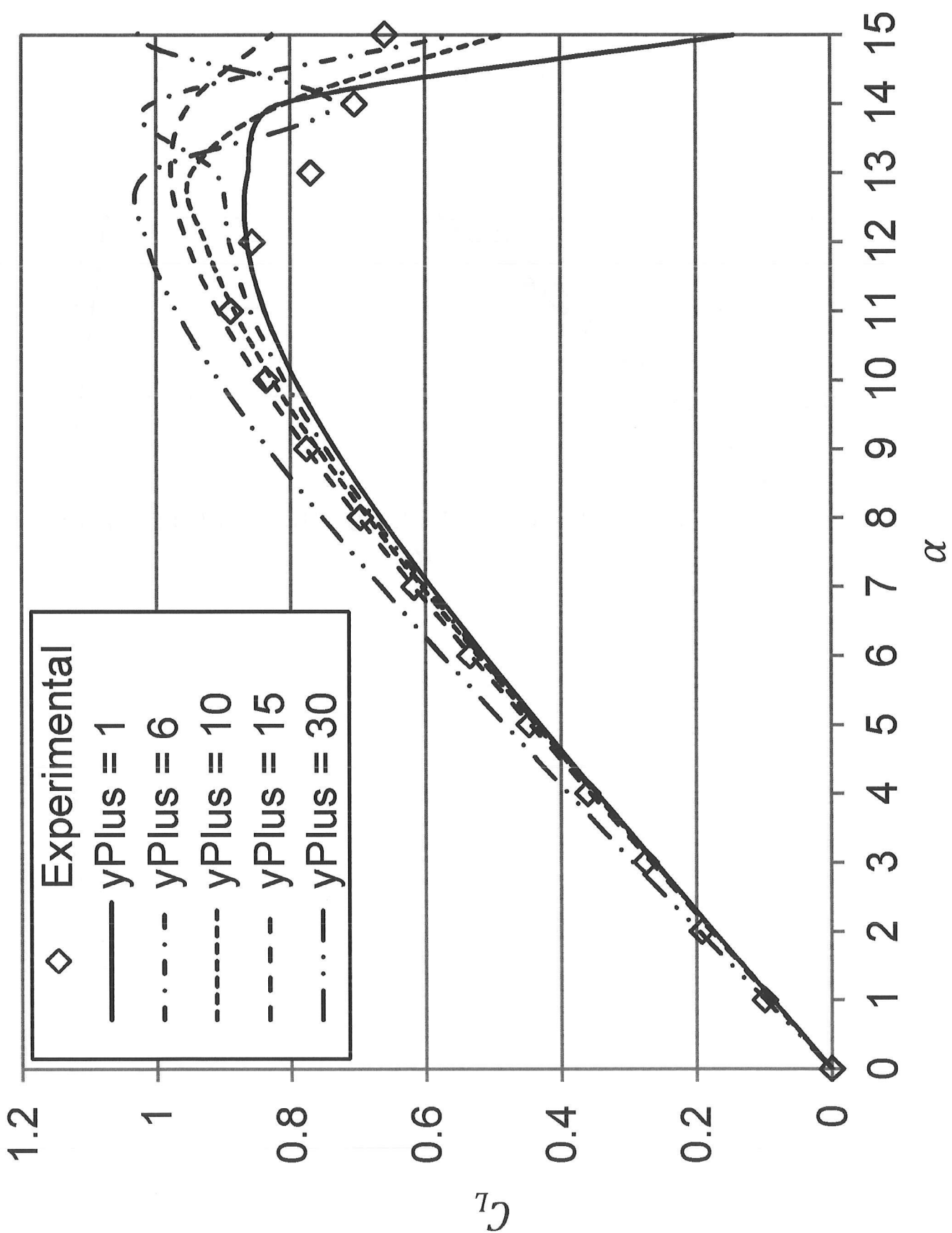


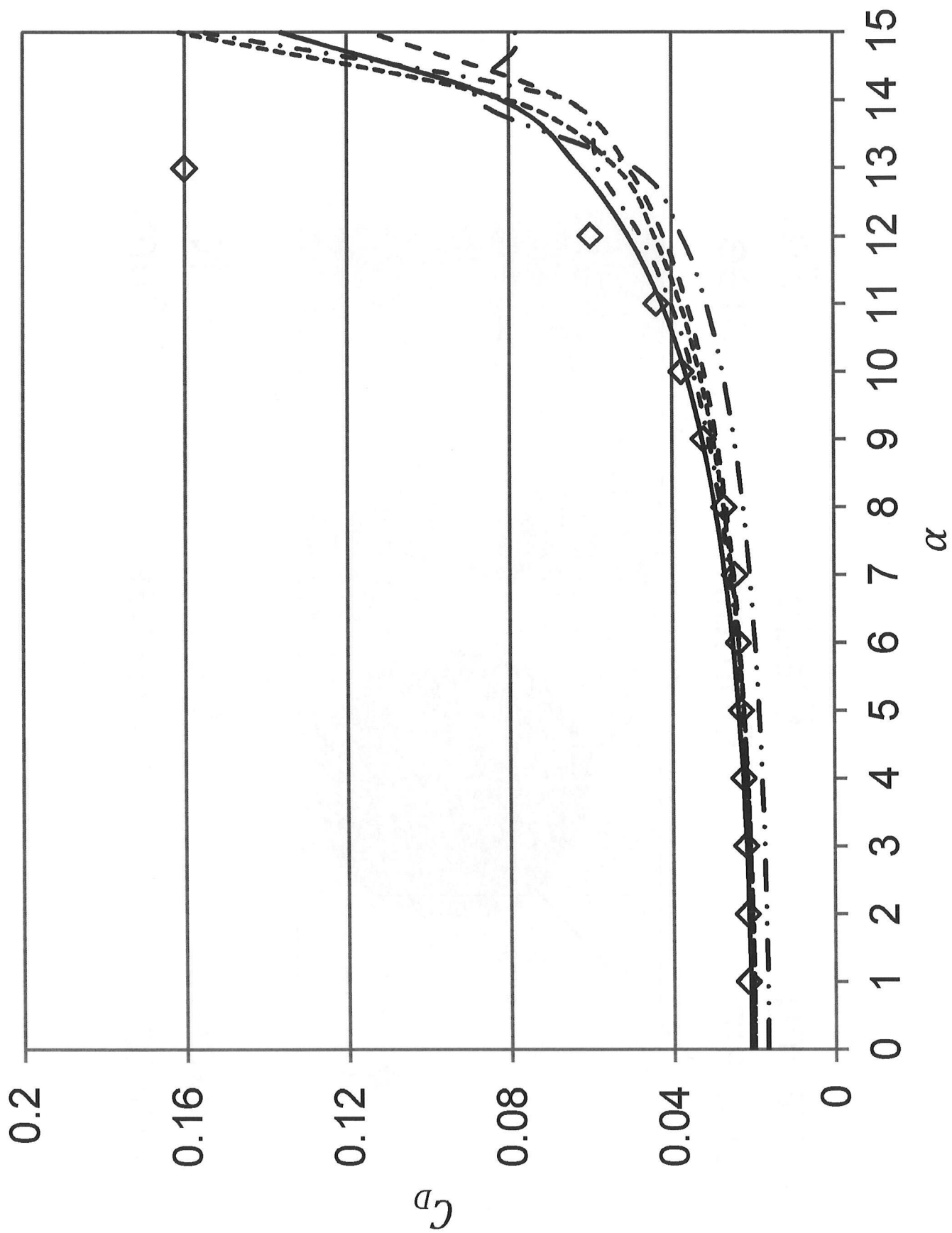




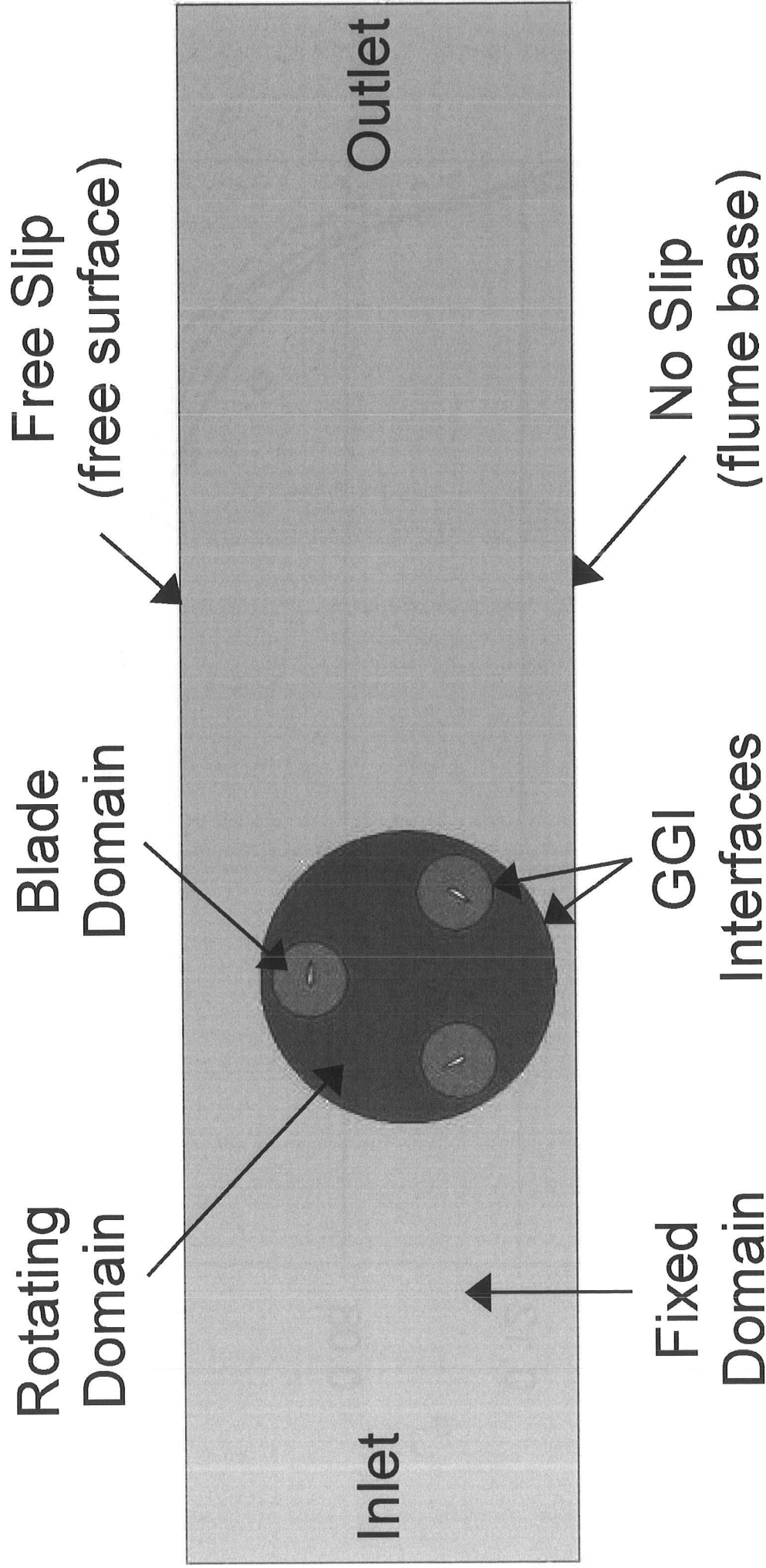


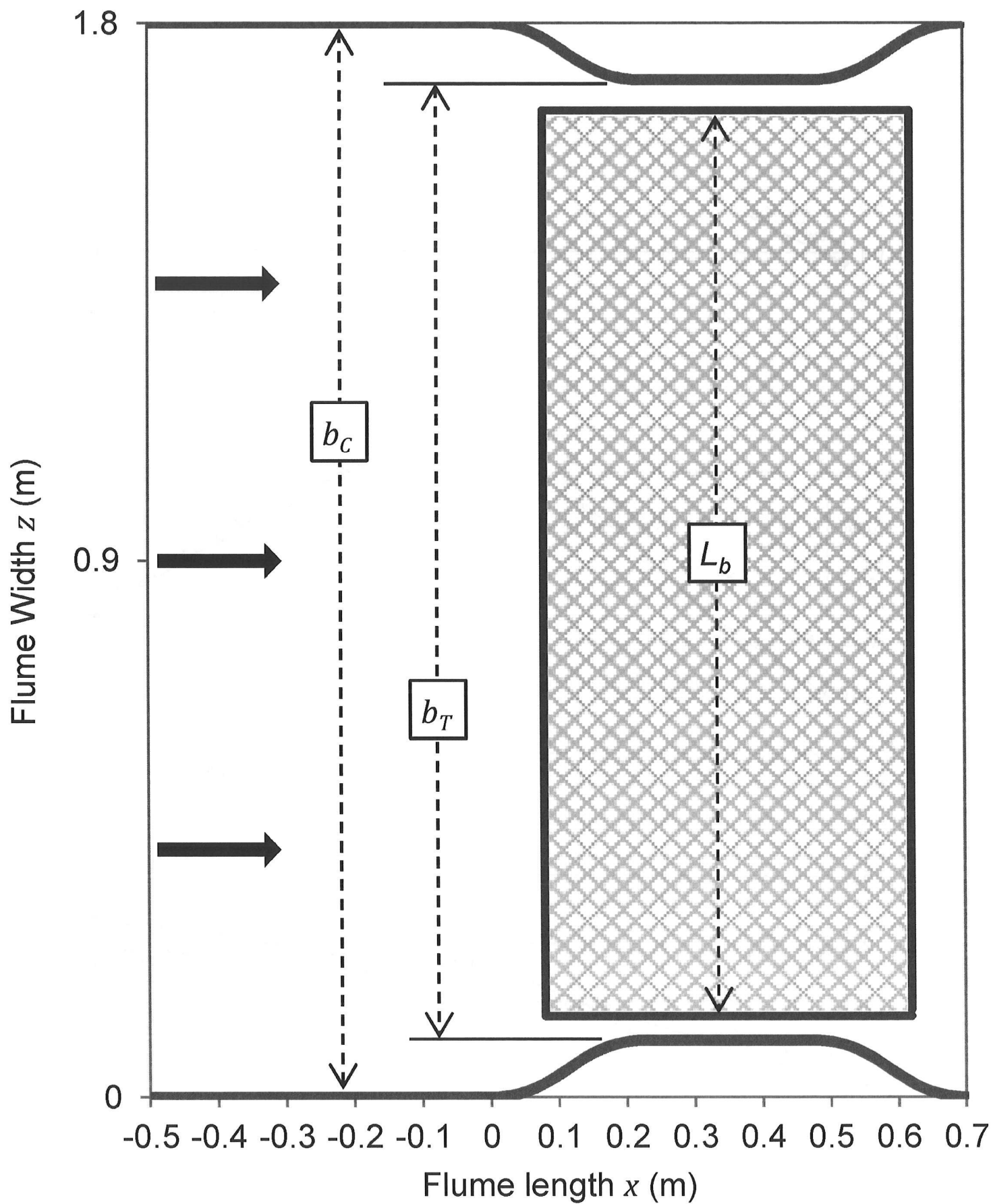


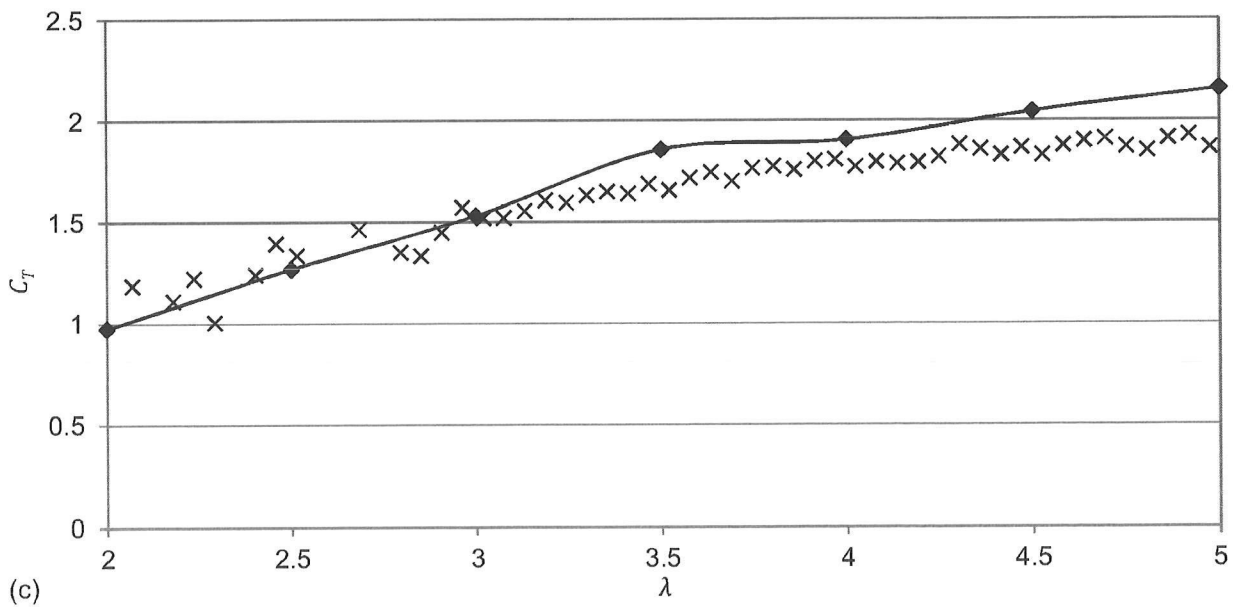
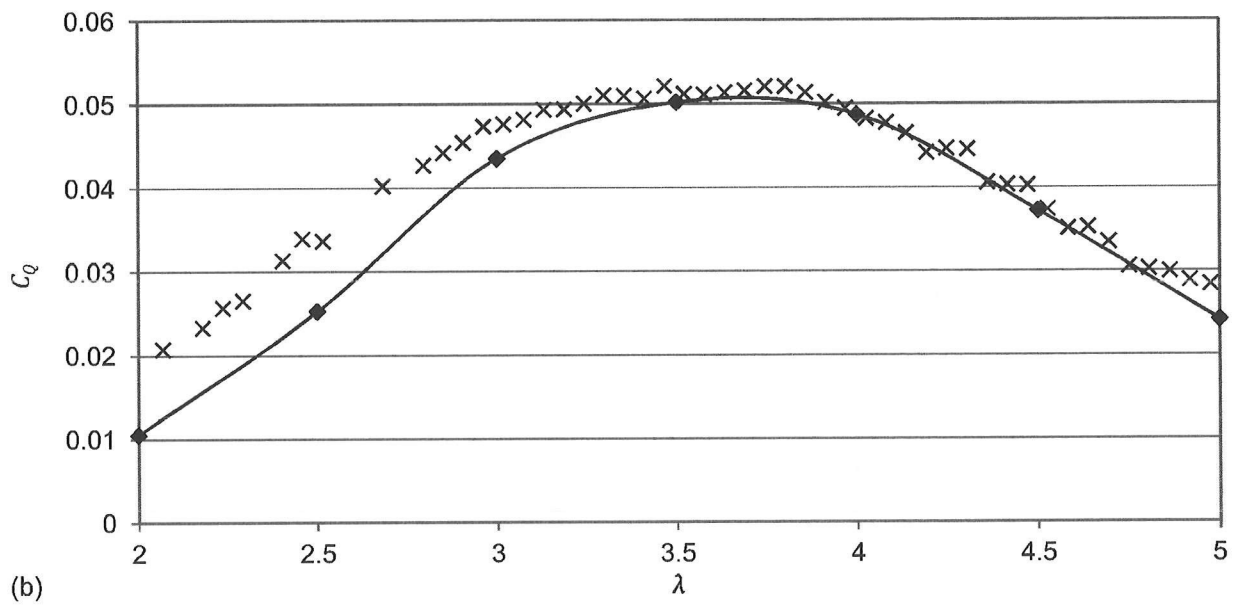
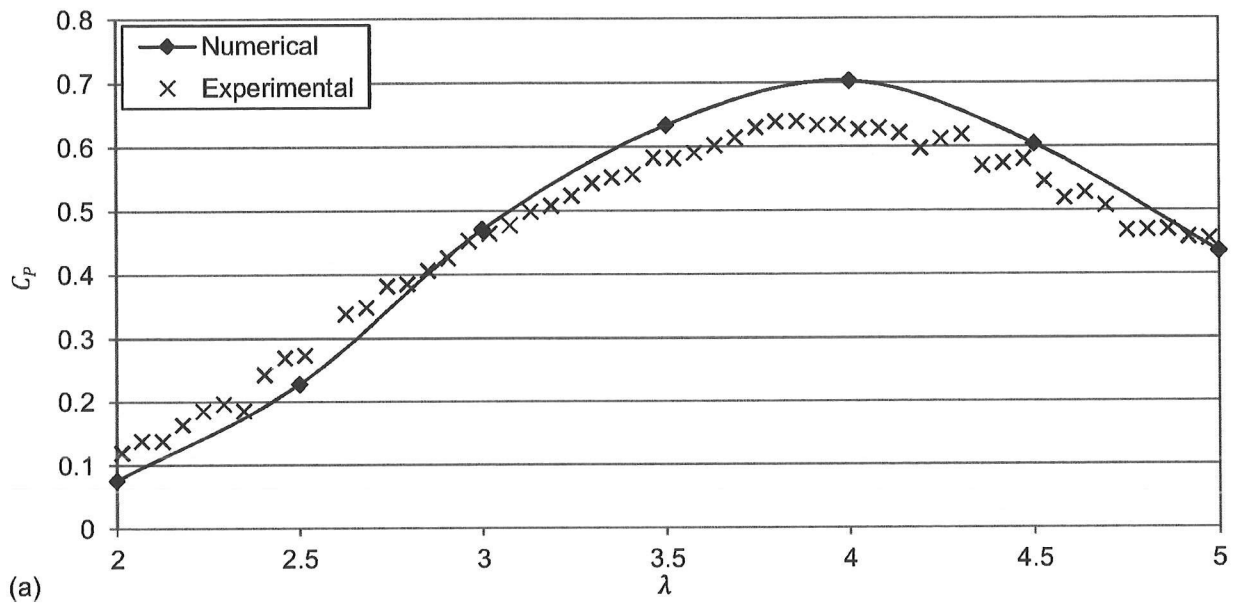


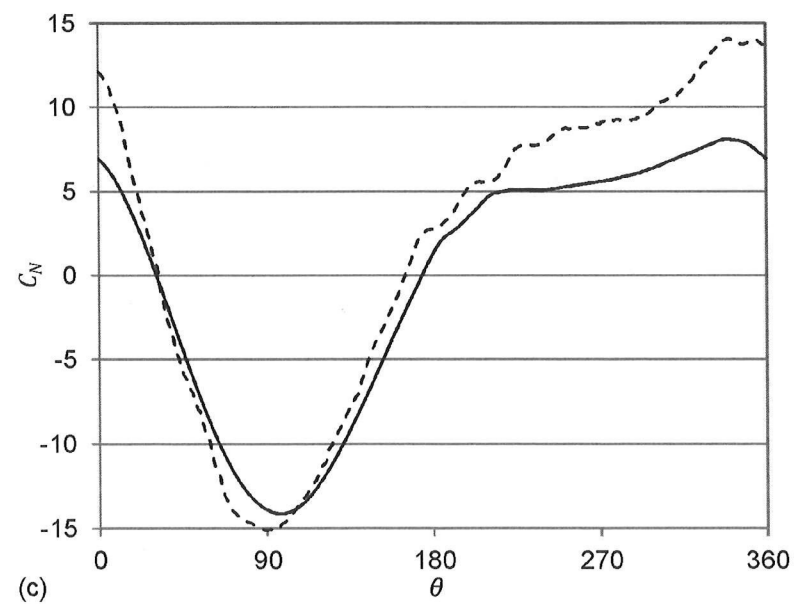
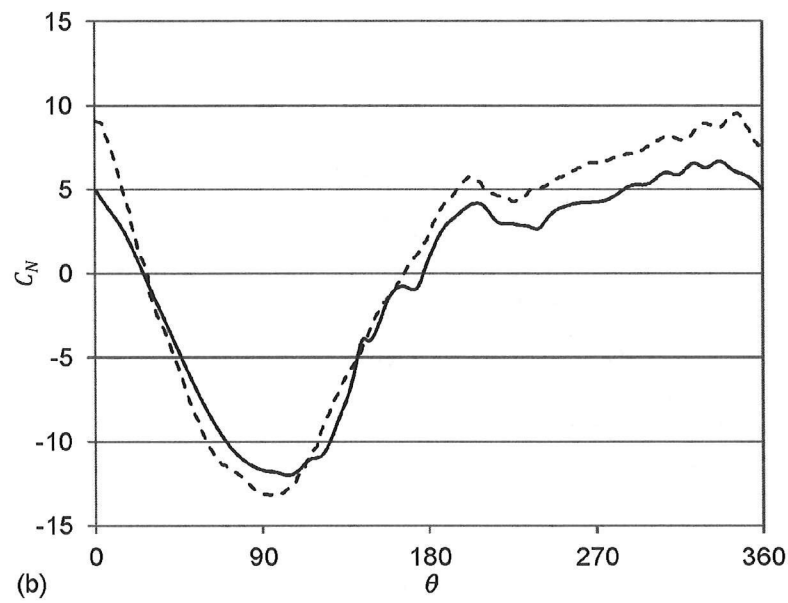
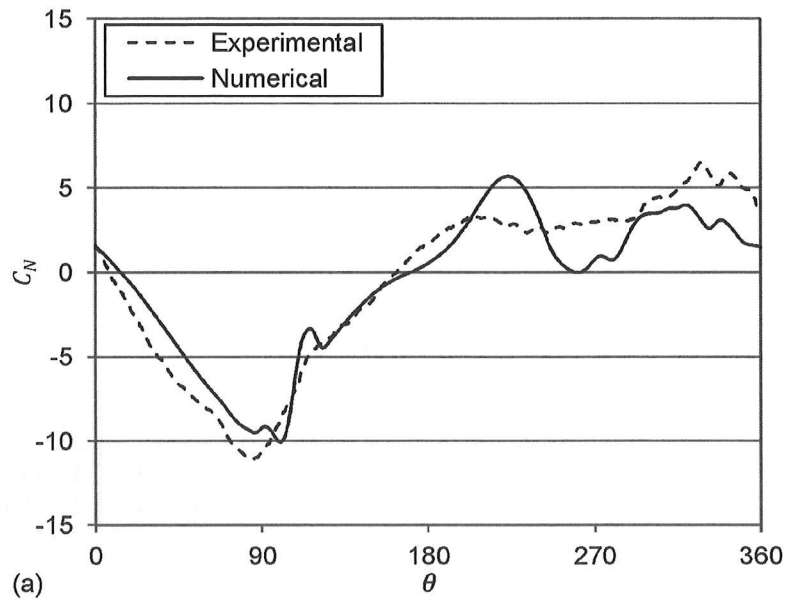


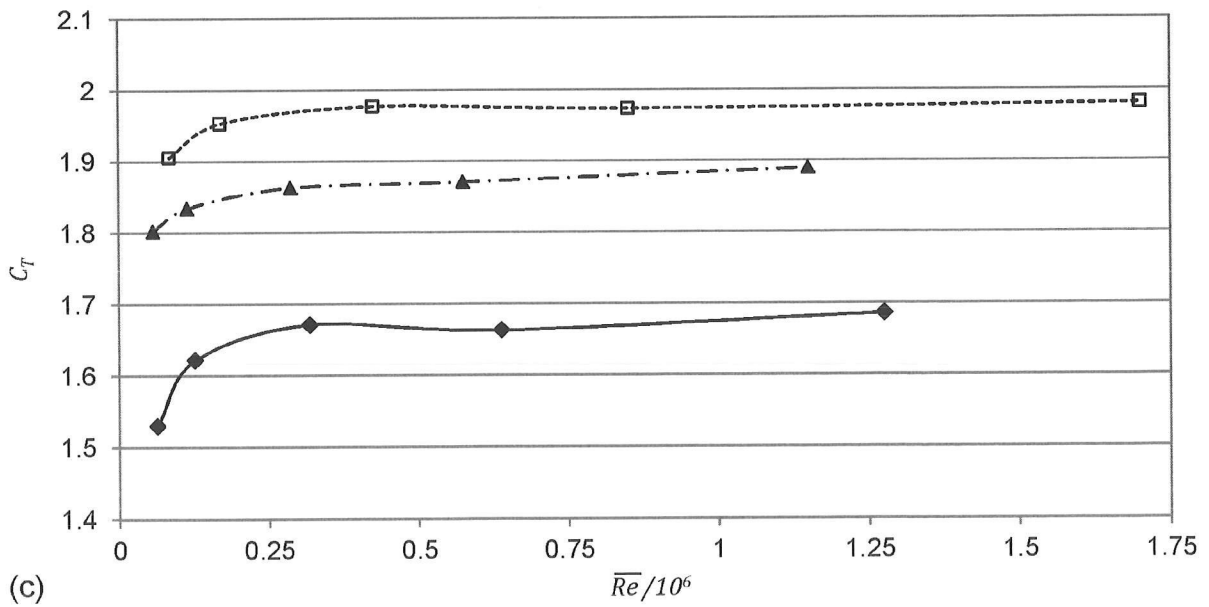
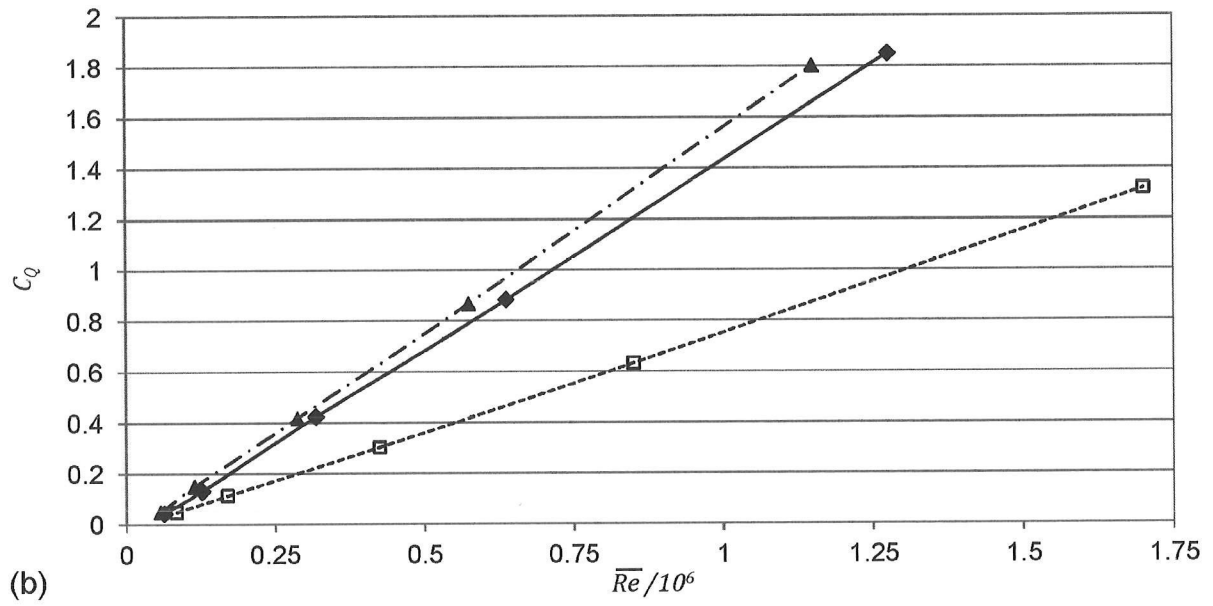
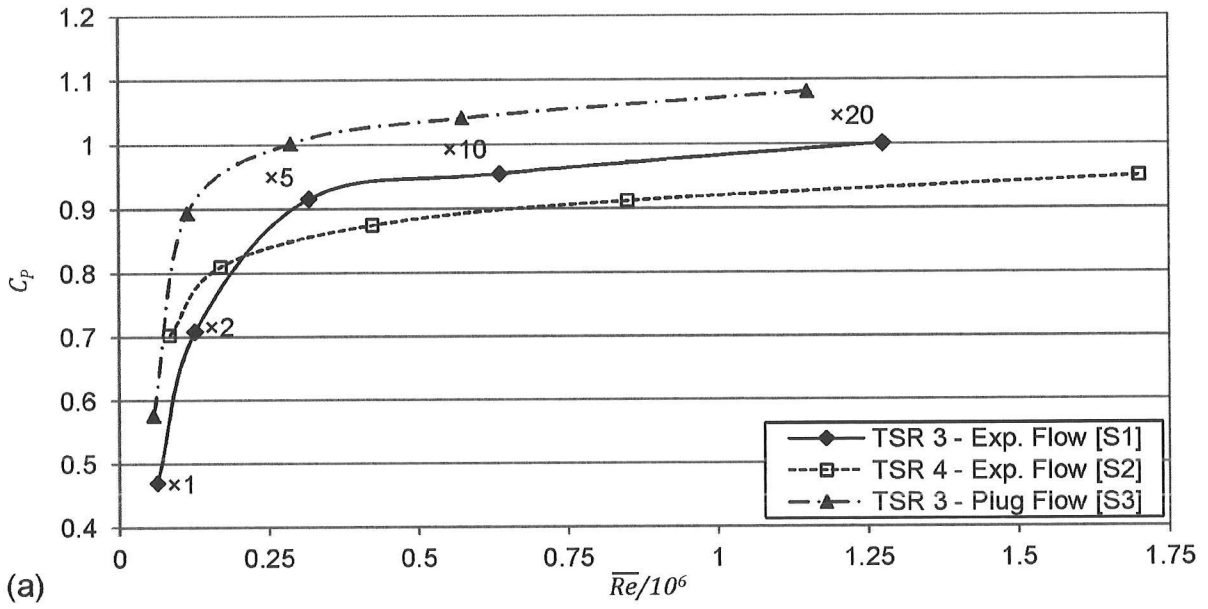


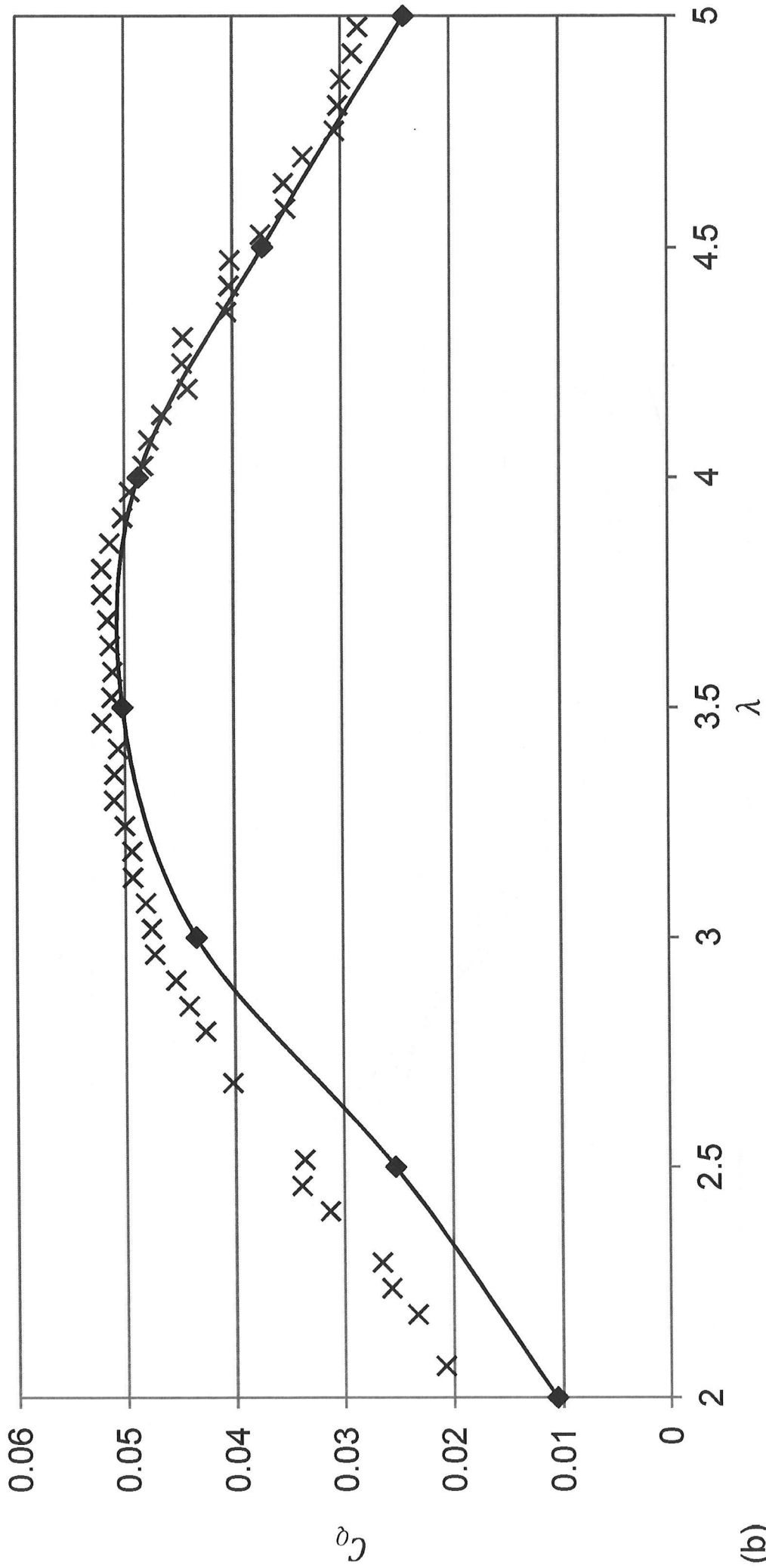




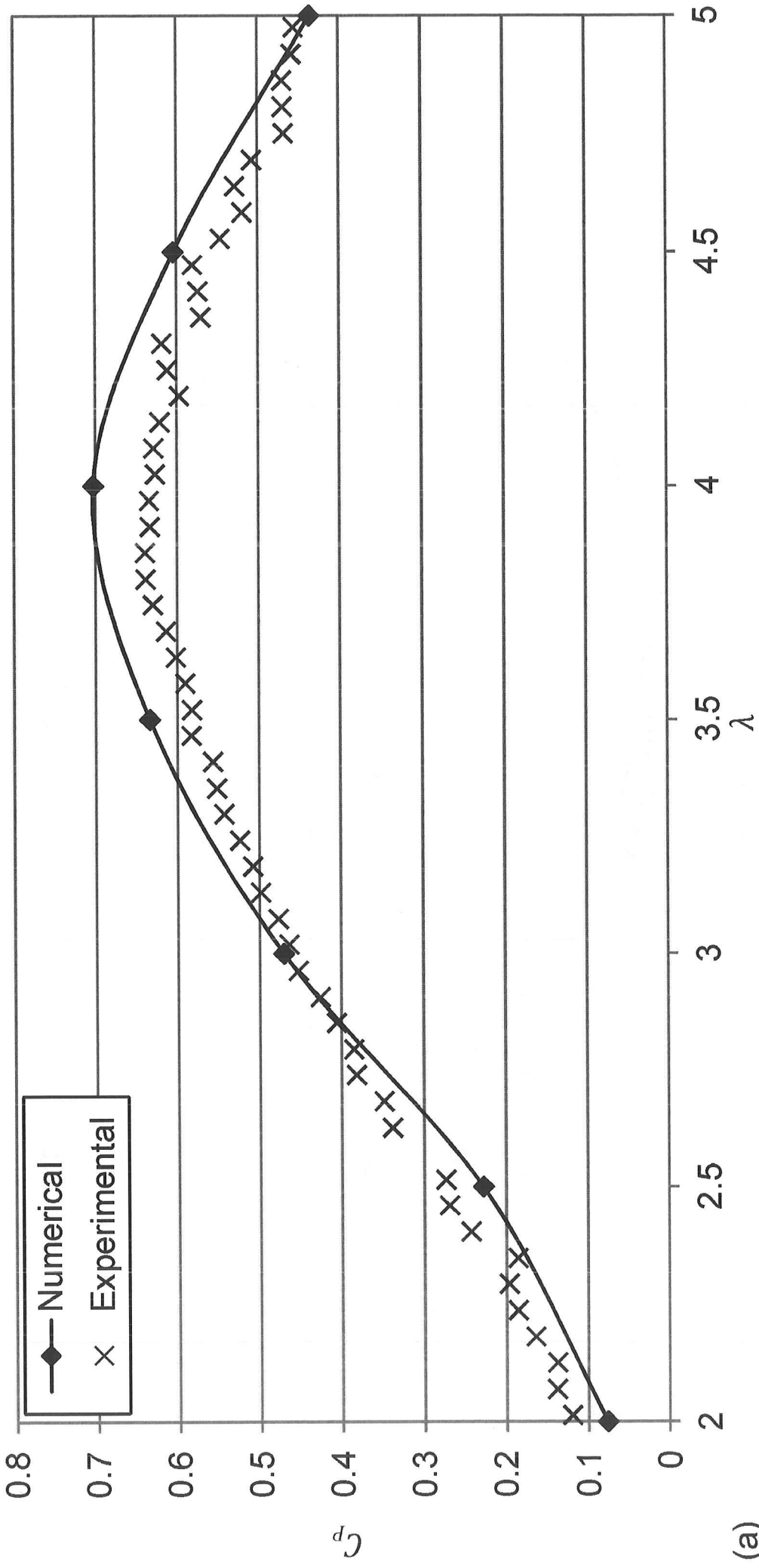




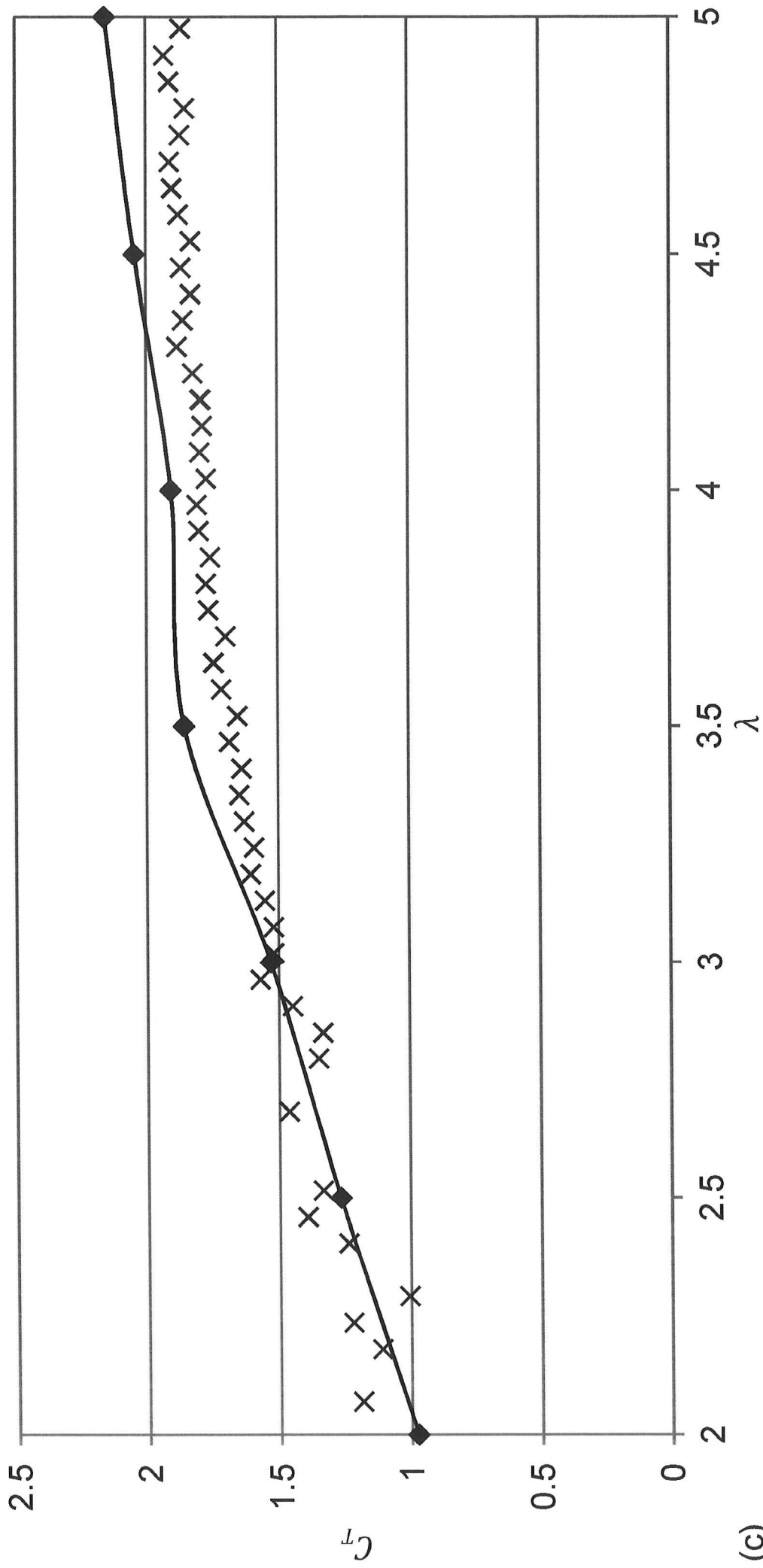




(b)



(a)



(c)



